

JLAB2 DataAnalysisHub

V.D. Burkert^{ak}, L. Elouadrhiri^{ak}, K.P. Adhikari^z, S. Adhikari^k, M.J. Amarian^{ae}, D. Anderson^{ak},
G. Angelini^l, H. Atac^{aj}, S. Aune^d, H. Avakian^{ak}, C. Ayerbe Gayoso^{ar,z}, N. Baltzell^{ak}, L. Barionⁿ,
M. Battaglieri^{p,ak}, V. Baturin^{ak}, I. Bedlinskiy^{aa}, F. Benmokhtar^h, A. Bianconi^{an,s}, A.S. Biselliⁱ, F. Bossù^d,
S. Boyarinov^{ak}, W.J. Briscoe^l, W.K. Brooks^{al}, K. Bruhwel^{ak}, D.S. Carman^{ak}, A. Celentano^p,
G. Charles^{t,ae}, P. Chatagnon^t, S. Christo^{ak}, T. Chetryz^{ad}, G. Christiaens^{ao,d}, G. Ciullo^{n,j}, B.A. Clary^f,
P.L. Cole^{x,m}, M. Contalbrigoⁿ, R. Cruz-Torres^y, C. Cuevas^{ak}, A. D'Angelo^{q,ag}, N. Dashyan^{as}, R. De Vita^p,
M. Defurne^d, A. Deur^{ak}, S. Diehl^f, C. Djalali^{ad,ai}, G. Dodge^{ae}, R. Dupre^t, M. Ehrhart^{a,t}, L. El Fassi^z,
R. Fair^{ak}, G. Fedotov^{ad}, A. Filippi^r, T.A. Foresttm, M. Garçon^d, G. Gavalian^{ak}, G.P. Gilfoyle^{af},
K. Giovanetti^v, F.X. Girod^{ak}, D.I. Glazier^{ao}, E. Golovatch^{ah}, R.W. Gothe^{ai}, Y. Gotra^{ak}, K.A. Griffioen^{ar},
M. Guidal^t, K. Hafidi^a, H. Hakobyan^{al,as}, C. Hanretty^{ak}, N. Harrison^{ak}, M. Hattawy^{ae,a}, F. Hauenstein^{ae},
T.B. Hayward^{ar}, D. Heddle^{e,ak}, P. Hemler^{ak}, O.A. Hen^y, K. Hicks^{ad}, A. Hobart^t, M. Holtrop^{ab}, Y. Ilieva^{ai},
I. Illari^l, D. Insley^{ak}, D.G. Ireland^{ao}, B.S. Ishkhanov^{ah}, E.L. Isupov^{ah}, H.S. Jo^w, K. Joo^f, S. Joosten^{a,aj},
T. Kageya^{ak}, D. Kashy^{ak}, C. Keith^{ak}, D. Keller^{aq}, M. Khachatryan^{ae}, A. Khanal^k, A. Kim^f, C.W. Kim^l,
W. Kim^w, V. Kubarovsky^{ak}, S.E. Kuhn^{ae}, L. Lanza^q, A. Lung^{ak}, M.L. Kabir^z, M. Leali^{an,s}, P. Lenisaⁿ,
K. Livingston^{ao}, M. Lowry^{ak}, I. J.D. MacGregor^{ao}, I. Mandjavidze^d, D. Marchand^t, N. Markov^f,
V. Mascagna^{am,s,an}, B. McKinnon^{ao}, M. McMullen^{ak}, C. Mealer^{ak}, M.D. Mestayer^{ak}, Z.E. Mezziani^{a,aj},
R. Miller^{ak}, T. Mineeva^{al}, M. Mirazita^o, V. Mokeev^{ak}, A. Movsisyanⁿ, C. Munoz Camacho^t, P. Naidoo^{ao},
S. Nanda^z, J. Newton^{ae}, S. Niccolai^t, G. Niculescu^v, M. Osipenko^p, M. Paolone^{aj}, L.L. Pappalardoⁿ,
R. Paremuzyan^{ab}, O. Pastor^{ak}, E. Pasyuk^{ak}, W. Phelps^{e,l}, O. Pogorelko^{aa}, J. Poudel^{ae}, J.W. Price^b,
K. Price^t, Y. Prok^{ae}, B.A. Raue^{k,ak}, M. Ripani^p, J. Ritman^u, A. Rizzo^{q,ag}, P. Rossi^{ak}, J. Rowley^{ad},
B.J. Roy^u, F. Sabatié^d, C. Salgado^{ac}, S. Schadmand^u, A. Schmidt^{y,l}, E.P. Segarra^y, V. Sergeyeva^t,
Y.G. Sharabian^{ak}, U. Shrestha^{ad}, Iu. Skorodumina^{ai,ah}, G.D. Smith^l, L.C. Smith^{l,ak}, D. Sokhan^{ao},
O. Soto^{o,al}, N. Sparveris^{aj}, P. Stoler^l, S. Strauch^{ai}, J.A. Tan^w, D. Tilles^{ak}, M. Turisini^o, N. Tyler^{ai},
M. Ungaro^{ak}, L. Venturelli^{an,s}, H. Voskanyan^{as}, E. Voutier^t, D. Watts^{ap}, X. Wei^{ak}, L.B. Weinstein^{ae},
C. Wiggins^{ak}, M.H. Wood^c, A. Yegneswaran^{ak}, G. Young^{ak}, N. Zachariou^{ap}, M. Zarecky^{ak}, J. Zhang^{aq},
Z.W. Zhao^{g,ae}, V. Ziegler^{ak}

^aArgonne National Laboratory, Argonne, Illinois 60439

^bCalifornia State University, Dominguez Hills, Carson, CA 90747

^cCanisius College, Buffalo, NY 14208

^dIRFU, CEA, Université Paris-Saclay, F-91191 Gif-sur-Yvette, France

^eChristopher Newport University, Newport News, Virginia 23606

^fUniversity of Connecticut, Storrs, Connecticut 06269

^gDuke University, Durham, North Carolina 27708

^hDuquesne University, Pittsburgh, PA 15282

ⁱFairfield University, Fairfield CT 06824

^jUniversità di Ferrara, 44121 Ferrara, Italy

^kFlorida International University, Miami, Florida 33199

^lThe George Washington University, Washington, DC 20052

^mIdaho State University, Pocatello, Idaho 83209

ⁿINFN, Sezione di Ferrara, 44100 Ferrara, Italy

^oINFN, Laboratori Nazionali di Frascati, 00044 Frascati, Italy

^pINFN, Sezione di Genova, 16146 Genova, Italy

^qINFN, Sezione di Roma Tor Vergata, 00133 Rome, Italy

^rINFN, Sezione di Torino, 10125 Torino, Italy

^sINFN, Sezione di Pavia, 27100 Pavia, Italy

^tInstitut de Physique Nucléaire, IN2P3-CNRS, Université Paris-Sud, Université Paris-Saclay, F-91406 Orsay, France

^uInstitute für Kernphysik (Juelich), 52428 Juelich, Germany

^vJames Madison University, Harrisonburg, Virginia 22807

^wKyungpook National University, Daegu 41566, Republic of Korea

^xLamar University, Beaumont, Texas 77710

^yMassachusetts Institute of Technology, Cambridge, Massachusetts 02139

^zMississippi State University, Mississippi State, MS 39762

^{aa}National Research Centre Kurchatov Institute - ITEP, Moscow, 117259, Russia

^{ab}University of New Hampshire, Durham, New Hampshire 03824

^{ac}Norfolk State University, Norfolk, Virginia 23504
^{ad}Ohio University, Athens, Ohio 45701
^{ae}Old Dominion University, Norfolk, Virginia 23529
^{af}University of Richmond, Richmond, Virginia 23173
^{ag}Universita' di Roma Tor Vergata, 00133 Rome Italy
^{ah}Skobeltsyn Institute of Nuclear Physics, Lomonosov Moscow State University, 119234 Moscow, Russia
^{ai}University of South Carolina, Columbia, South Carolina 29208
^{aj}Temple University, Philadelphia, PA 19122
^{ak}Thomas Jefferson National Accelerator Facility, Newport News, Virginia 23606
^{al}Universidad Técnica Federico Santa María, Casilla 110-V Valparaíso, Chile
^{am}Università degli Studi dell'Insubria, 22100 Como, Italy
^{an}Università degli Studi di Brescia, 25123 Brescia, Italy
^{ao}University of Glasgow, Glasgow G12 8QQ, United Kingdom
^{ap}University of York, York YO10 5DD, United Kingdom
^{aq}University of Virginia, Charlottesville, Virginia 22901
^{ar}College of William and Mary, Williamsburg, Virginia 23187
^{as}Yerevan Physics Institute, 375036 Yerevan, Armenia

Abstract

The CEBAF Large Acceptance Spectrometer for operation at 12 GeV beam energy (CLAS12) in Hall B at Jefferson Laboratory is used to study electro-induced nuclear and hadronic reactions. This spectrometer provides efficient detection of charged and neutral particles over a large fraction of the full solid angle. CLAS12 has been part of the energy-doubling project of Jefferson Lab's Continuous Electron Beam Accelerator Facility, funded by the United States Department of Energy. An international collaboration of over 40 institutions contributed to the design and construction of detector hardware, developed the software packages for the simulation of complex event patterns, and commissioned the detector systems. CLAS12 is based on a dual-magnet system with a superconducting torus magnet that provides a largely azimuthal field distribution that covers the forward polar angle range up to 35°, and a solenoid magnet and detector covering the polar angles from 35° to 125° with full azimuthal coverage. Trajectory reconstruction in the forward direction using drift chambers and in the central direction using a vertex tracker results in momentum resolutions of <1% and <3%, respectively. Cherenkov counters, time-of-flight scintillators, and electromagnetic calorimeters provide good particle identification. Fast triggering and high data-acquisition rates allow operation at a luminosity of $10^{35} \text{ cm}^{-2}\text{s}^{-1}$. These capabilities are being used in a broad program to study the structure and interactions of nucleons, nuclei, and mesons, using polarized and unpolarized electron beams and targets for beam energies up to 11 GeV. This paper gives a general description of the design, construction, and performance of CLAS12.

Keywords: CLAS12, Magnetic spectrometer, Electromagnetic physics, Large Acceptance, JLab

1. Introduction

Electron scattering has proven an effective way of probing the size and internal structure of subatomic particles such as protons, neutrons, and nuclei. Exploiting energetic electron beams led to rapid progress in our understanding of the internal composition of particles. The extended size of the proton was first mapped out in the mid-1950's [1], and the internal quark substructure was discovered in the late 1960's [2]. Using spin-polarized electrons and spin-polarized targets, the internal quark helicity momentum distribution was mapped out in the 1980's and the following decades, and is still an important research topic today [3]. These experiments required only inclusive measurements, where only the beam particle, electrons or muons, that scattered off the target were detected and kinematically analyzed.

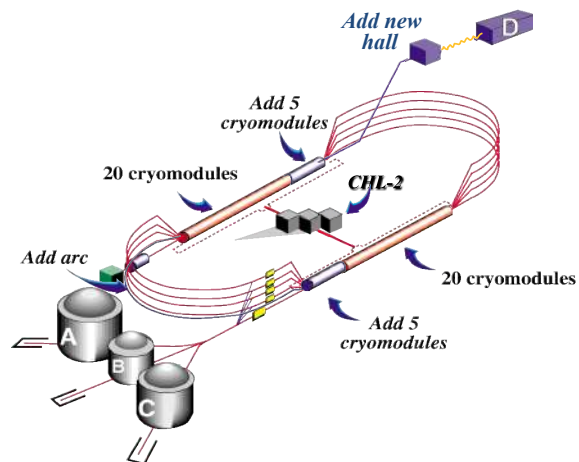


Figure 1: The CEBAF continuous electron beam accelerator after the doubling of the beam energy to 12 GeV and adding Hall D as a new experimental end station for photon physics experiments. The accelerator is 1,400 m in circumference.

In the decades following these discoveries, it was realized that a more detailed understanding of the internal structure of nucleons requires the reconstruction of fully exclusive or semi-inclusive processes, and hence the detection and kinematical reconstruction of additional mesons and baryons in the final state was required. Other constraints came from the need of baryon spectroscopy to measure

complete angular distributions, which made it necessary to employ large acceptance devices to serve that purpose. The Continuous Electron Beam Accelerator Facility (CEBAF) [4], the CLAS detector [5], and other experimental equipment at Jefferson Laboratory (JLab) were designed and constructed in the 1990's with these goals in mind and were operated successfully for over 15 years.

The further development of Quantum Chromodynamics (QCD) as the theory of the interaction of colored quarks and gluons, combined with the discovery of the Generalized Parton Distributions (GPDs), provided a novel way that allowed describing the nucleon structure in 3 dimensions (3D), 2 in coordinate space and 1 in momentum space. The discovery opened up a new avenue of hadronic research that has become one of the flagship programs in nuclear and hadronic physics. The GPDs must be probed in exclusive processes, with deeply virtual Compton scattering being the most suitable one. This is a rather rare process and measurements require the operation of large acceptance detectors at high instantaneous luminosities of $10^{35} \text{ cm}^{-2} \text{ s}^{-1}$ to map out the process in the full kinematic phase space using polarized beams, polarized targets, and sufficiently high beam energy. The complementary process of semi-inclusive deep inelastic scattering (SIDIS) is also of topical interest to probe the internal structure of the nucleon in 3D momentum space. The science program of CLAS12 is very broad [6] and encompasses the study of the structure of the proton and neutron both in their ground state, as well as their many excited states, and in the deeply inelastic kinematics. Other experiments are designed to probe the short range structure of nuclei through measurements of the transparency of nuclei to mesons and baryons, and how it changes with the momentum transfer.

2. The JLab Facility at 12 GeV

The CLAS12 detector was designed to study electro-induced nuclear and hadronic reactions by providing efficient detection of charged and neutral particles over a large fraction of the full solid angle. A collaboration of over 40 institutions has participated in the design, fabrication, assembly, and final commissioning of CLAS12 in Hall B at Jefferson Laboratory. The CLAS12 detector is based on a combination of a six-coil torus magnet and a high-field solenoid magnet. The combined magnetic field provides a large coverage in both azimuthal

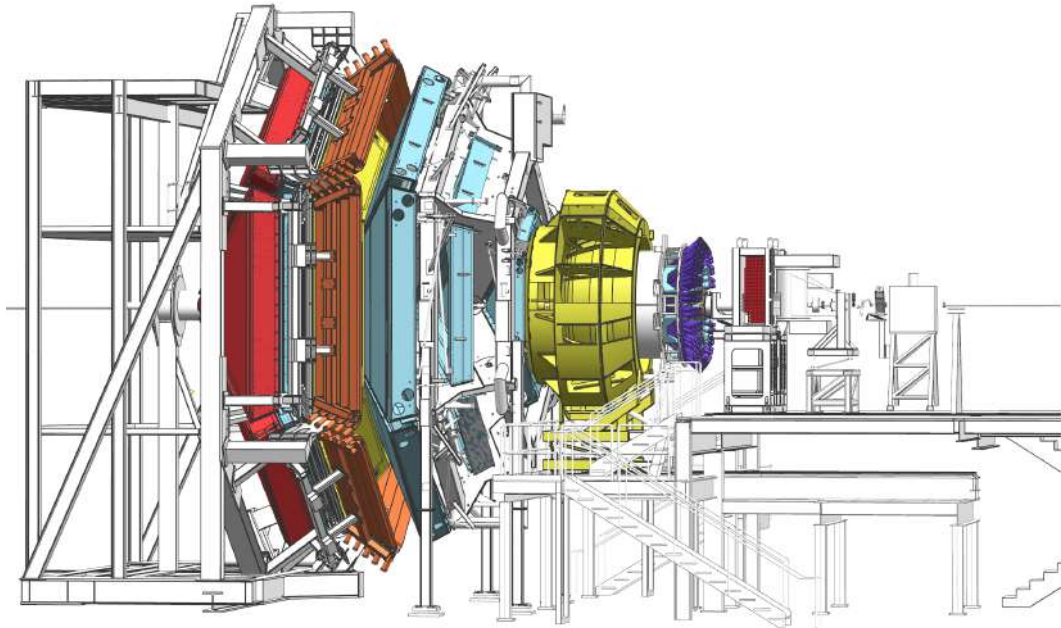


Figure 2: The CLAS12 detector in the Hall B beamline. The electron beam enters from the right and impinges on the production target located in the center of the solenoid magnet shown at the right (upstream) end of CLAS12, where other detector components are also visible. Scattered electrons and forward-going particles are detected in the Forward Detector (FD) consisting of the High Threshold Cherenkov Counter (HTCC) (yellow) with full coverage in polar angle $5^\circ \leq \theta \leq 35^\circ$ and $\Delta\phi = 2\pi$ coverage in azimuth. The HTCC is followed by the torus magnet (gray), the drift chamber tracking system (light blue), another set of Cherenkov counters (hidden), time-of-flight scintillation counters (brown), and electromagnetic calorimeters (red). Between the HTCC and the torus, the Forward Tagger is installed to detect electrons and photons at polar angles $2^\circ \leq \theta \leq 5^\circ$. The Central Detector (CD) consists of the Silicon Vertex Tracker (hidden), which is surrounded by a Barrel Micromesh Tracker (hidden), the Central Time-of-Flight system, and the Central Neutron Detector (PMTs in blue). At the upstream end, a Back Angle Neutron Detector (red) is installed. In the operational configuration, the entire CLAS12 detector extends for 13 m along the beamline.

152 and polar angles. Trajectory reconstruction using 173
 153 drift chambers at forward angles results in a mo- 174
 154 mentum resolution of $\sigma_p/p \approx 0.7\%$. At large polar 175
 155 angles, where particle momenta are typically be- 176
 156 low 1 GeV, the momentum resolution is $\sigma_p/p \approx$ 177
 157 3.5%. Cherenkov counters, time-of-flight systems, 178
 158 and calorimeters provide good particle identifica- 179
 159 tion for electrons, charged pions, kaons, and pro- 180
 160 tons. Fast triggering and high data acquisition rates 181
 161 allow operation at luminosities of $10^{35} \text{ cm}^{-2}\text{s}^{-1}$ for 182
 162 extended periods of time. These capabilities are be- 183
 163 ing used in a broad scientific program to study the 184
 164 structure and interactions of baryons, mesons, and 185
 165 nuclei using polarized and unpolarized targets. 186

166 This paper provides a general description of the 187
 167 design, construction, and performance of CLAS12 188
 168 and how it expands upon the capabilities provided 189
 169 by the JLab 12 GeV energy upgrade. The CEBAF 190
 170 accelerator and experimental halls are shown for 191
 171 the energy upgraded configuration in Fig. 1. CE- 192
 172 BAF is designed from two parallel linear accel-

173 ators (linacs) based on superconducting radio fre-
 174 quency (RF) technology, and arranged in a race-
 175 track configuration [4]. Spin-polarized electrons are
 176 generated in the gun, pre-accelerated in the injec-
 177 tor, and subsequently injected and accelerated in
 178 the north linac. They are then bent in a 180° arc
 179 and injected into the south linac. This is repeated
 180 four and a half more times to reach the final en-
 181 ergy for Hall D and up to four times for the desired
 182 delivery energies to Halls A, B, and C. In the re-
 183 circulating arcs, electrons are transported in 5 in-
 184 dependent out-of-phase tracks of different energies.
 185 For 12 GeV operation, five accelerating cryomod-
 186 ules with four times higher gradients than were used
 187 in the 6 GeV CEBAF machine were added to each
 188 of the two existing linacs to reach a maximum en-
 189 ergy of 11 GeV for Halls A, B, and C. One added
 190 arc path and one more pass through the north linac
 191 were added to achieve the highest beam energy of
 192 12 GeV for Hall D. This highest beam energy is gen-
 193 erated exclusively for Hall D, while the other three

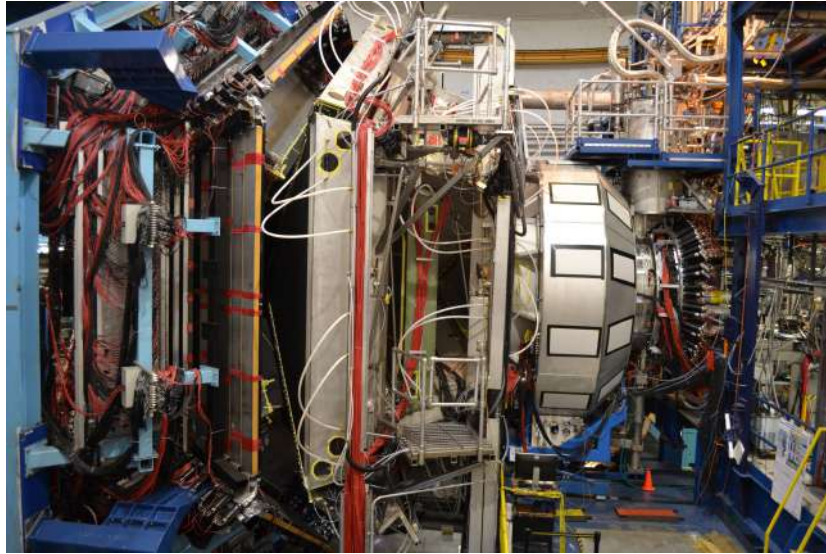


Figure 3: The CLAS12 detector in the Hall B beamline. The beam enters from the right near the upstream end of the solenoid magnet and the cryogenic service tower, followed by the HTCC and the torus magnet with the drift chambers. The Low Threshold Cherenkov Counter, Forward Time-of-Flight, and the electromagnetic calorimeters (PCAL and EC) are seen at the downstream end to the left.



Figure 4: The CLAS12 magnet systems. Left: The fully assembled solenoid magnet including all cryogenic connections on the beamline at the beginning of cool down, before the detector installation. Right: The torus magnet with all six coils mechanically assembled in a common cryostat. The coil cryostat, which is fabricated from non-magnetic steel, has an outside width of 124 mm. The cross bars provide a cold (4.5 K) cryogenic connection of neighboring coils, and counteract the out-of-plane forces to provide mechanical stability to the full magnet. Due to the large physical size of the assembled torus magnet, the final assembly of the magnet had to be completed in Hall B.

194 halls may receive beams at the same beam energy 195 or at different beam energies simultaneously, with

up to a factor of 10^5 differences in current from 1 nA to 100 μ A.

Major new detectors and other experimental equipment have been installed in Halls B, C, and D that support a broad science program addressing fundamental issues in nuclear and hadronic physics. In Hall D, a large hermetic detector with a solenoid magnet at its core has been in operation since 2015. It incorporates tracking capabilities and photon detection over nearly the full 4π solid angle. This hall is dedicated to the production of mesons employing a linearly polarized photon beam. The new CLAS12 spectrometer, displayed in a side view in Fig. 2 (from the design model) and in Fig. 3 (photograph), features large solid angle coverage and instantaneous luminosities of 10^{35} $\text{cm}^{-2}\text{s}^{-1}$ for electron scattering experiments with multiple particle final states.

Hall C includes the new super-high momentum magnetic spectrometer (SHMS) in addition to the existing high momentum spectrometer. In Hall A, a new super big bite spectrometer (SBS) has been added to the existing high resolution spectrometer pair HRS², and other large installation experiments have been proposed. Complementing the new equipment is the highly spin-polarized electron gun, high-power cryogenic targets, and several spin-polarized targets using NH_3 , ND_3 , HD, ^3He , and ^7Li as target materials to support a broad range of polarization measurements.

3. The CLAS12 Superconducting Magnets

The design of CLAS12 is based on a combination of a toroidal magnetic field at polar angles up to $\approx 35^\circ$ and a 5 T solenoidal field in the central region in the approximate polar angle range $35^\circ \leq \theta \leq 125^\circ$. The primary requirement driving this choice is the ability to measure charged particles at high momentum with good resolution at forward angles, while operating the detector systems at high luminosity. This requires effective shielding of the detector system from low-energy electrons produced in the target material due to Møller scattering $e^- + e^- \rightarrow e^- + e^-$ of the high-energy beam electrons on atomic electrons in the target material. The large majority of those electrons are prevented from reaching the sensitive detectors as they curl up in the strong longitudinal magnetic field, and are then guided into a shielding pipe made from bulk tungsten material where they dump their en-

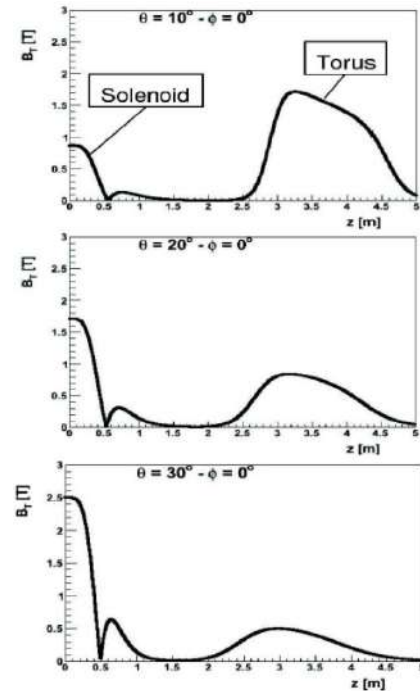


Figure 5: Combined solenoid and torus magnetic fields, showing the magnetic field component perpendicular to the radial distance from the solenoid center. Only the transverse components act on the charged tracks. At small polar angles the particle deflecting component is small in the solenoid field, while it is largest in the torus magnet. For large polar angle the transverse component is large in the solenoid field and small in the torus field volume.

245 ergy. The fully assembled torus and solenoid mag-
 246 nets are shown in Fig. 4.

247 The distribution of the absolute magnetic field
 248 along lines of constant polar angle seen from the
 249 target position is shown in Fig. 5. Both the torus
 250 and solenoid magnetic fields are included. The field
 251 distributions of the solenoid and torus magnets are
 252 shown in Fig. 6.

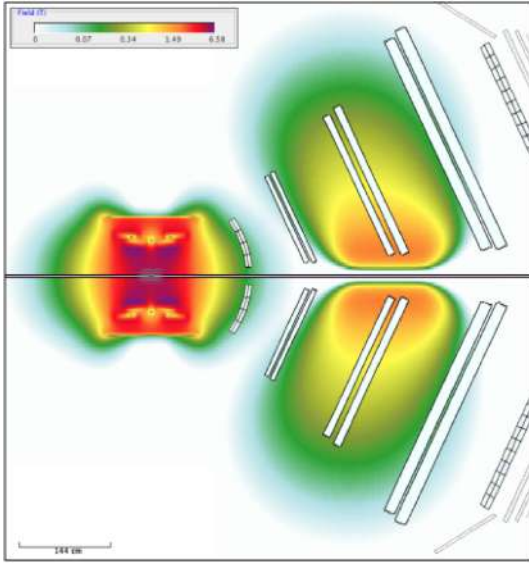


Figure 6: Combined solenoid and torus magnetic fields. The color code shows the total magnetic field of both the solenoid and torus at full current. The open boxes indicate the locations and dimensions of the active detector elements.

253 3.1. The Torus Magnet

254 A contour of one of the six identical coils of the
 255 torus magnet is shown in Fig. 7. The geometri-
 256 cal coverage as seen from the target ranges from 5°
 257 to 40° in polar angle. The symmetrically arranged
 258 six magnet coils provide an approximate toroidal
 259 magnetic field around the beamline. The six coils
 260 are mounted in a central cold hub on a common
 261 stainless-steel cylinder, which also provides the ge-
 262 ometrical symmetry for the alignment of the coils
 263 near the magnet center (see Fig. 8). This increases
 264 placement accuracy of the coil packages in areas
 265 where the magnetic field is expected to be maxi-
 266 mal. A full view of the assembled torus coils and
 267 cryostat is shown in Fig. 4(right). The open range
 268 in azimuthal angle depends on the polar angle of
 269 the particle trajectory, and ranges from 50% of 2π
 270 at 5° to about 90% of 2π at 40° .

271 Each superconducting coil is made from a two-
 272 coil “double-pancake” potted in an aluminum case.
 273 The number of windings per pancake is 117. The
 274 conductor is Superconducting Super Collider outer
 275 dipole cable soldered into a $20\text{ mm} \times 2.5\text{ mm}$ cop-
 276 per channel with a turn-to-turn insulation of $75\ \mu\text{m}$
 277 fiberglass tape. Operating at a nominal current of
 278 3770 A, the peak field is 3.58 T at the inner turns
 279 close to the warm bore. For symmetry reasons the
 280 field on the beam axis is ideally equal to zero, with
 281 a small remnant field present due to imperfections
 282 in the magnet assembly and coil positions. The
 283 $\int Bdl$ at the nominal current is 2.78 Tm at 5° and
 284 0.54 Tm at 40° . The inductance of the magnet is
 285 2.0 H and the stored energy 14.2 MJ. The magnet
 286 has liquid- N_2 cooled heat shields. After assembly
 287 and cool down, the magnet reached full field imme-
 288 diately. For details on the design and operation of
 289 the torus magnet, see Ref. [7].

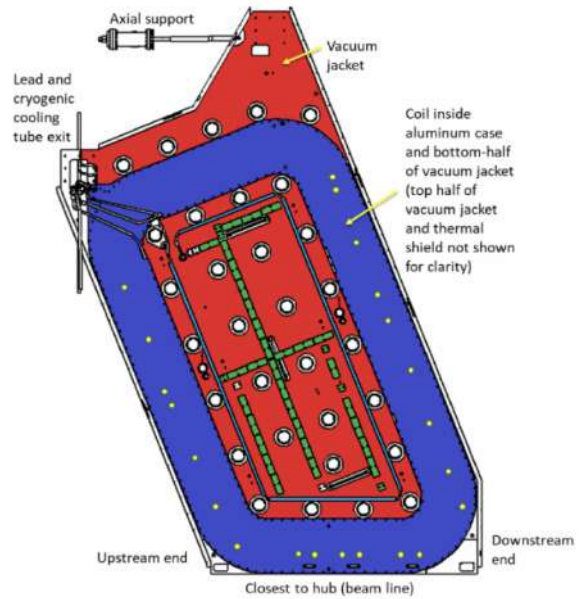


Figure 7: A torus magnet coil (blue) in its vacuum jacket. All six coils are nominally identical to each other, and are tilted forward at a 22° angle relative to the vertical, and are symmetrically arranged in azimuth. The height of the coil package is 0.3 m and the entire coil spans about $2\text{ m} \times 4\text{ m}$.

290 3.2. The Solenoid Magnet

291 The solenoid magnet is a self-shielded supercon-
 292 ducting magnet around the beamline used to gener-
 293 ate a field primarily in the beam direction. Figure 9
 294 shows the design layout of the solenoid coils, and
 295 the fully assembled magnet is shown in Fig. 4(left).

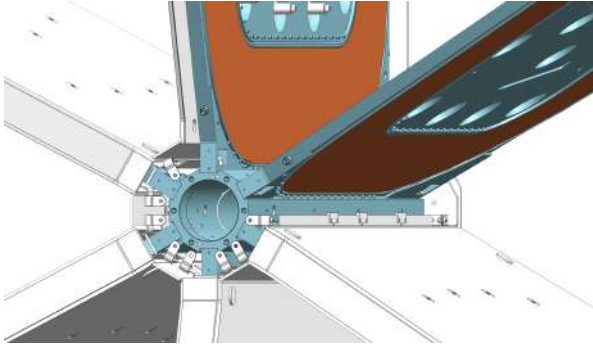


Figure 8: The six torus coils are mounted on the cold central stainless-steel hub that bears the centripetal force. The dark-shaded areas indicate the location of the superconducting coils, surrounded by the cryostat and vacuum jacket.

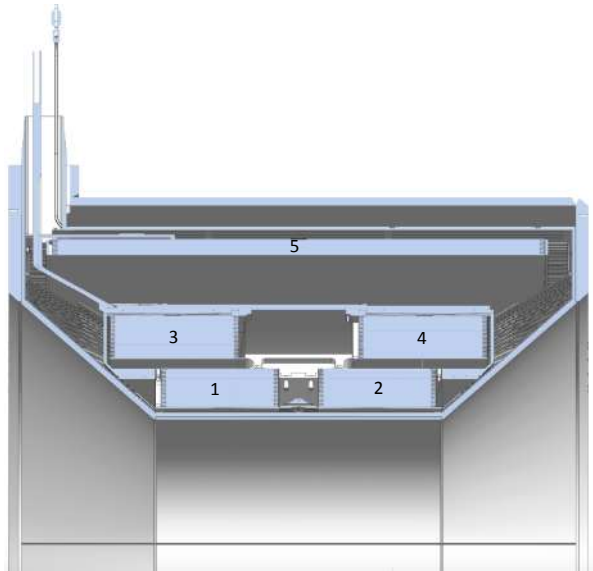


Figure 9: Cut view of the upper half of the solenoid coils with the four 2×2 main coils on the inside, and the shield coil (5) on the outside. The shield coil provides effective compensation for the magnetic field sensitive photomultiplier tubes that are located just outside of the magnet cryostat (not shown). The nominal field in the center of the magnet is 5 T.

The design is driven by the physics requirements to (a) provide a magnetic field for particle tracking at large angles, (b) act as a Møller electron shield, and (c) provide a highly uniform field at the magnet center for the operation of dynamically polarized proton and deuteron targets. Figure 10 shows the moment when the magnets had reached their full design currents. Figure 11 shows the correlation of solenoid field strength vs. current up to (and slightly beyond) the maximum current.

The magnet consists of 4 cylindrical coils arranged in two packages at different radial distances to the beamline. A fifth coil is located outside of the 4 inner coils and generates a magnetic field in the opposite direction of the field of the 4 inner coils and thus acts as an active magnetic shield. The number of turns in the main coils is 3704 ($2 \times 840 + 2 \times 1012$) and in the shield coil is 1392. The magnet is powered at a nominal current of 2416 A. At full current the solenoid generates a 5 T magnetic field at its center. The integrated field length along the magnet center is $\int Bdl = 7.0 \text{ Tm}$, generating a stored energy of 20 MJ. The magnet has an inner warm bore of 78 cm diameter where all of the central detectors are placed. For details on the design and operation of the solenoid magnet, see Ref. [7].

4. The CLAS12 Forward Detector (FD)

4.1. Drift Chamber (DC)

The six coils of the torus magnet mechanically support the forward tracking system, which consists of three independent DCs in each of the six sectors of the torus magnet. Each of the six DC sectors has a total of 36 layers with 112 sense wires, arranged in 3 regions (R1, R2, and R3) of 12 layers each. In each of the six torus sectors the DCs are arranged identically. As displayed in Fig. 12, the R1 chambers are located at the entrance to the torus magnetic field region, the R2 chambers are located inside the magnet where the magnetic field is close to its maximum, and the R3 chambers are placed in a low magnetic field space just downstream of the torus magnet. This arrangement provides independent and redundant tracking in each of the six torus sectors. Each of the 3 regions consists of 6 layers (called a superlayer) with wires strung at a stereo angle of $+6^\circ$ with respect to the sector midplane and 6 layers (a second superlayer) with wires strung at a stereo angle of -6° with respect to the sector midplane. This stereo view enables excellent resolution in the most important polar angle (laboratory scattering angle), and good resolution in the less critical azimuthal scattering angle. Figure 13 shows the wire stringing operation for the large R3 chambers. For details of the DC construction and performance, see Ref. [8].

4.2. Particle Identification

Cherenkov counters, time-of-flight detectors, and electromagnetic calorimeters are located downstream

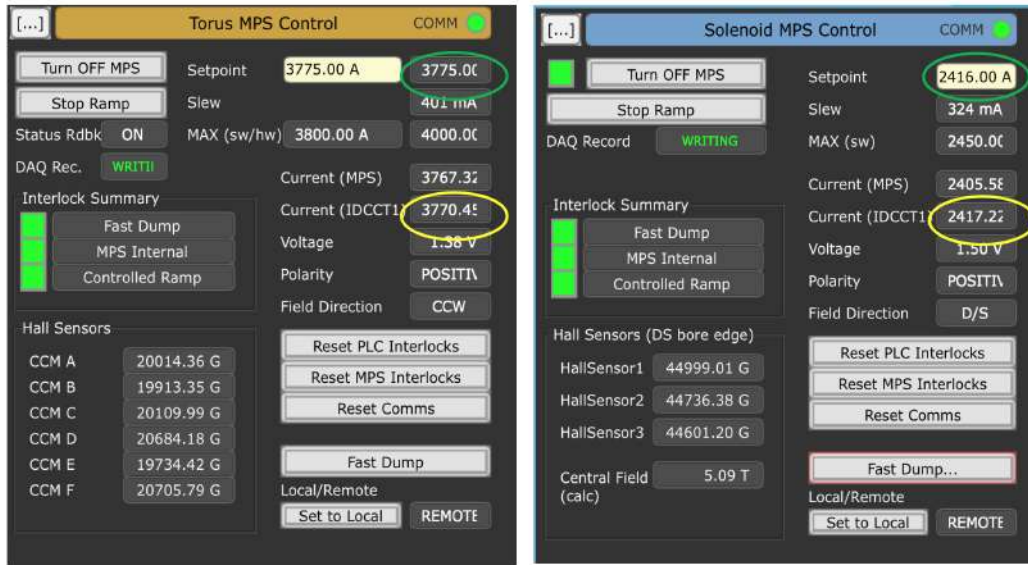


Figure 10: Energization of the torus magnet (left) and the solenoid magnet (right) to full current.

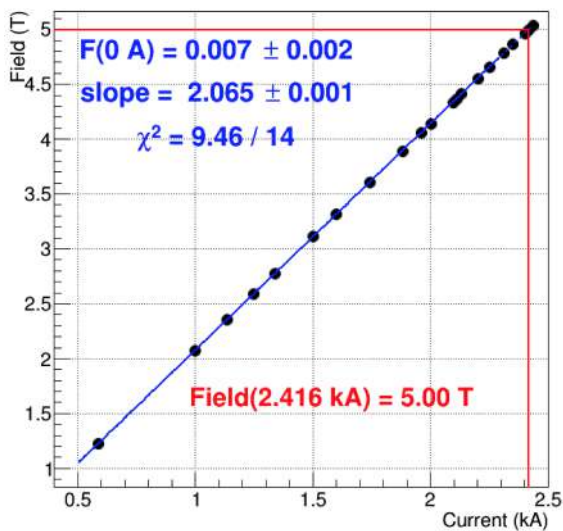


Figure 11: The excitation line of the solenoid to full current. The nominal field in the center of the solenoid magnet is 5.0 T.

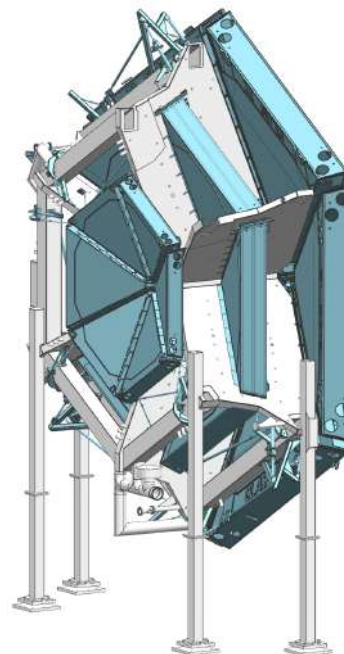


Figure 12: Drift chamber system in the CLAS12 forward tracking system from the design model. The small-size R1 chambers are located just in front of the torus magnet coils (gray shade). The medium-size R2 chambers are sandwiched between the coils of the magnet, and the large-size R3 chambers are located just downstream of the magnet.

354 of the tracking system to provide particle identifica-
 355 tion and energy measurements for electrons, high-
 356 energy photons, and neutrons. Each is described in
 357 more detail in the remainder of this section.

358 4.3. High Threshold Cherenkov Counter (HTCC)

359 The HTCC is the main detector to separate
 360 electrons (positrons) with momenta below 4.9 GeV

361 from charged pions, kaons, and protons. The detec-
 362 tor has full coverage of 360° in azimuth and spans



Figure 13: Simultaneous wire stringing of two R3 chambers in the Jefferson Lab clean room.

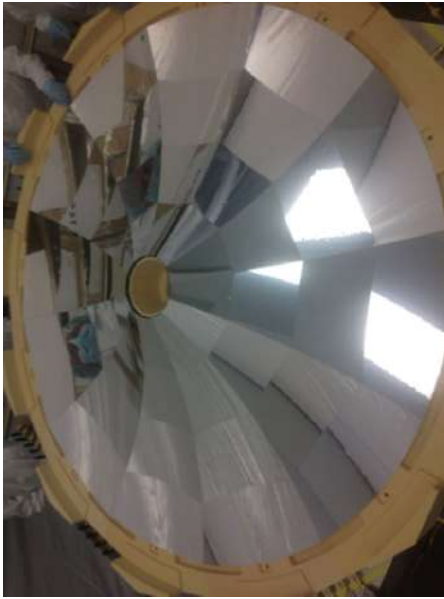


Figure 14: The HTCC mirror with its 48 mirror facets, each reflecting the Cherenkov light to a different PMT. The mirror spans a diameter of about 2.4 m.

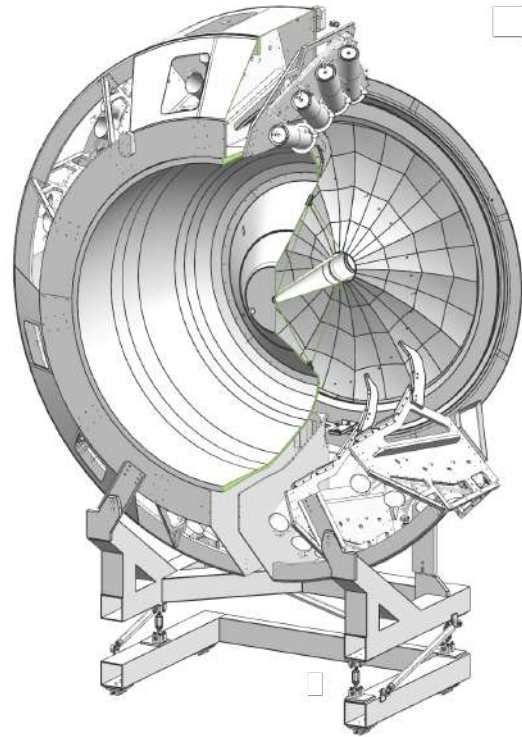


Figure 15: Cut view of the assembled HTCC detector. The container spans a diameter of about 4.5 m. The mirror is seen at the downstream end to the right. The PMTs are mounted in 12 sectors and in groups of 4 at the outer perimeter of the container. Light collection uses additional Winston cones and 5-in PMTs with quartz windows.

363 from 5° to 35° in polar angle. It has no blind areas
 364 in its complete solid angle coverage. The detector is
 365 located downstream of the production target, sand-
 366 wiced between the solenoid magnet and the torus
 367 magnet, in front of the forward tracking detectors.

368 The HTCC system is required to provide high 418
 369 rejection of charged pions and low background noise 419
 370 for reliable identification of scattered electrons in 420
 371 a dense electromagnetic background environment. 421
 372 The HTCC is a single unit operated in dry CO₂ 422
 373 gas at 1 atm pressure. It is constructed using a 423
 374 multi-focal mirror of 48 elliptical mirror facets that 424
 375 focuses the Cherenkov light on 48 photomultiplier 425
 376 tubes (PMTs) with quartz windows of 125-mm diam- 426
 377 eter. The PMTs are located in a magnetic field of 427
 378 up to 35 G oriented along the phototube axes and 428
 379 are surrounded along their lengths by a multi-layer
 380 magnetic shield with active compensation coils.

381 In order to minimize multiple scattering in the
 382 HTCC detector materials and to limit its impact
 383 on the momentum analysis of charged tracks in the
 384 torus field, the HTCC mirror system is constructed
 385 using a backing structure of low-density composite
 386 material. As the detector is located in front of the
 387 momentum analyzing torus magnet, all materials
 388 but the radiator gas in the path of the charged par-
 389 ticles had to be kept to a minimum. In the actual
 390 detector, the density of the solid material seen by
 391 charged particles passing through the HTCC vol-
 392 ume is 135 mg/cm².

393 The HTCC is also used to generate a fast sig-
 394 nal to be used as a trigger for scattered electrons.
 395 The HTCC operates in conjunction with energy de-
 396 posited in the electromagnetic calorimeters to iden-
 397 tify electrons of specific energies. The 360° mirror
 398 system of the HTCC is shown in Fig. 14. Figure 15
 399 shows a cut view of the assembled HTCC detector.
 400 For details of the HTCC construction and perfor-
 401 mance, see Ref. [9].

402 4.4. Low Threshold Cherenkov Counter (LTCC)

403 The LTCC system is part of the CLAS12 For-
 404 ward Detector and is used for charged pion detec-
 405 tion at momenta greater than 3.5 GeV. The LTCC
 406 system consists of boxes shaped like truncated pyra-
 407 mids. Four of the six sectors of CLAS12 are equip-
 408 ped with one LTCC box. Each LTCC box contains 108
 409 lightweight mirrors with composite backing struc-
 410 tures, 36 Winston light-collecting cones, 36 125-
 411 mm diameter PMTs, and 36 magnetic shields. The
 412 LTCC boxes are filled with heavy C₄F₁₀ radiator
 413 gas. The LTCC system has previously been used
 414 to detect electrons in the CLAS detector at lower
 415 energies [10]. It has been refurbished to provide
 416 higher efficiency for charged pion detection by in-
 417 creasing the volume of the radiator gas, refurbishing

the elliptical and hyperbolic mirrors with new coat-
 ings, and improving the sensitivity of the PMTs to
 Cherenkov light by coating their entrance windows
 with wavelength shifting material that absorbs ul-
 traviolet (UV) light at wavelength below 300 nm
 and re-emits two back-to-back photons at larger
 wavelength. The components of the LTCC opti-
 cal mirror system and its arrangement are shown
 in Figs. 16 and 17. For details of the LTCC con-
 struction, the detector refurbishment, and its per-
 formance, see Ref. [11].

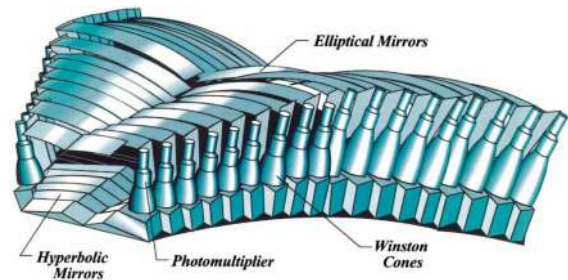


Figure 16: Layout and components of the optical mirror system within each LTCC box from the design model.

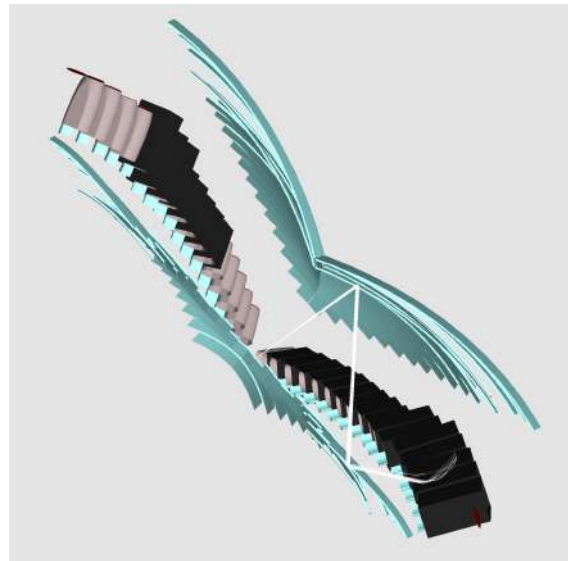


Figure 17: Perspective representation of the LTCC optical system. A charged particle enters from the bottom left and generates Cherenkov light in the radiator gas volume. The light is reflected off the elliptical mirror array towards the hyperbolic mirror array, from where it is reflected towards the Winston cone and 5-in PMT. The large acceptance coverage requires a complex mirror system for efficient light collection.

4.5. Ring Imaging Cherenkov Detector (RICH)

Some experiments require the detection and identification of charged kaons in momentum ranges that are not accessible with the standard time-of-flight method used with the Forward Time-of-Flight system, or with the LTCC Cherenkov counters. The time-of-flight resolution of the scintillators is no longer sufficient to separate kaons from pions for momenta greater than 3 GeV. For that purpose an additional RICH detector was built and incorporated into one of the CLAS12 sectors to replace the corresponding LTCC sector¹. The RICH detector is designed to improve CLAS12 particle identification in the momentum range 3-8 GeV. It incorporates aerogel radiators, visible light photon detectors, and a focusing mirror system that is used to reduce the detection area instrumented by photon detectors to 1 m².

Multi-anode photomultiplier tubes (MaPMTs) provide the required spatial resolution and match the aerogel Cherenkov light spectrum in the visible and near-UV region. For forward scattered particles ($\theta < 13^\circ$) with momenta 3 - 8 GeV, a proximity imaging method with thin (2 cm) aerogel and direct Cherenkov light detection is used. For larger incident particle angles of $13^\circ < \theta < 25^\circ$ and momenta of 3 - 6 GeV, the Cherenkov light is produced by a thicker aerogel layer of 6 cm, focused by a spherical mirror, and undergoes two further passes through the thin radiator material and a reflection from planar mirrors before detection. Figure 18 shows the RICH mirror system and Fig. 19 details the optics of the detector. For further details of the RICH detector construction and performance see Ref. [12].

4.6. Forward Time-of-Flight (FTOF)

The FTOF system is part of the Forward Detector and is used to measure the time-of-flight of charged particles emerging from the production target during beam operation. It includes six sectors of plastic scintillators with double-sided PMT readout. Each sector consists of three arrays of counters (panel-1a - 23 counters, panel-1b 62 counters, panel-2 5 counters). The system is required for excellent timing resolution for particle identification and good segmentation for flexible triggering options. The detectors span a range in polar angle

¹A second RICH module is presently under construction and will be installed into the final CLAS12 FD sector diametrically across from the first module

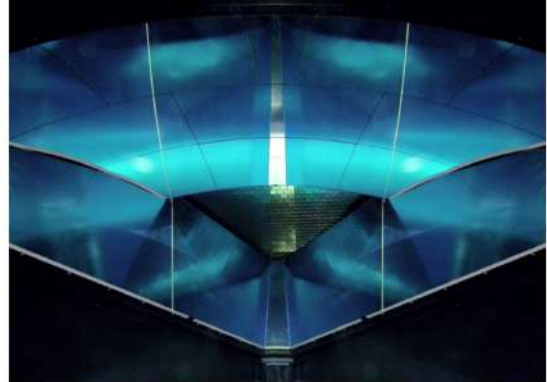


Figure 18: The RICH mirror system shown here in a perspective view as seen from the entrance window, with the spherical mirrors above, and the planar mirrors below. The detector array with the MaPMTs is seen in the center. The aerogel radiator is not shown.

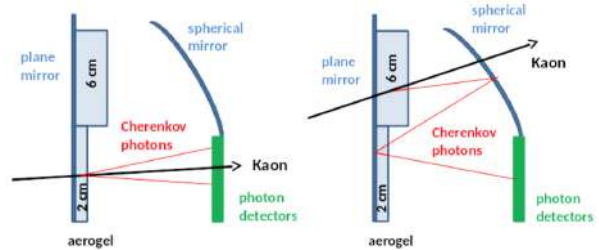


Figure 19: The principle of operation and the optics of the RICH detector. The left panel shows the optics for direct light detection and the right panel shows the optics for reflected light detection.

from 5° to 45° , covering 50% in ϕ at 5° and 90% at 45° . The lengths of the counters range from 32.3 cm to 376.1 cm in panel 1a, from 17.3 cm to 407.9 cm in panel-1b, and from 371.3 cm to 426.2 cm in panel-2. The average timing resolution in panel-1a is 125 ps, 85 ps in panel-1b, and 155 ps in panel-2. Figures 20 and 21 show the FTOF system on the Forward Carriage. For details of the FTOF construction and performance, see Ref. [13].

4.7. Electromagnetic Calorimeters (ECAL)

The CLAS12 detector package uses the existing electromagnetic calorimeter (EC) of the CLAS detector [14] and a new pre-shower calorimeter (PCAL) installed in front of the EC. Together the PCAL and EC are referred to as the ECAL. The calorimeters in CLAS12 are used primarily for the identification and kinematical reconstruction of electrons, photons (e.g. from $\pi^0 \rightarrow \gamma\gamma$ and $\eta \rightarrow \gamma\gamma$ decays), and neutrons. For details of the construction of

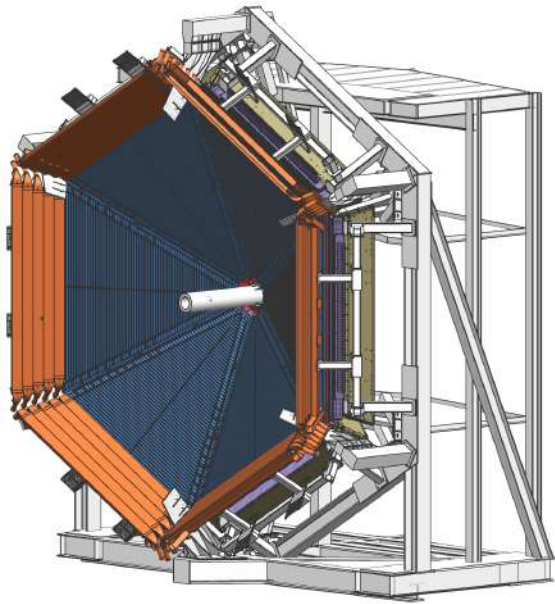


Figure 20: 3D rendering of the Forward Carriage with the FTOF system showing the panel-1b counters on the inside, and the panel-2 counters on the outside. The panel-1a counters are located immediately downstream of the panel-1b counters and are not visible here. Part of the PCAL is visible downstream of the FTOF panels.

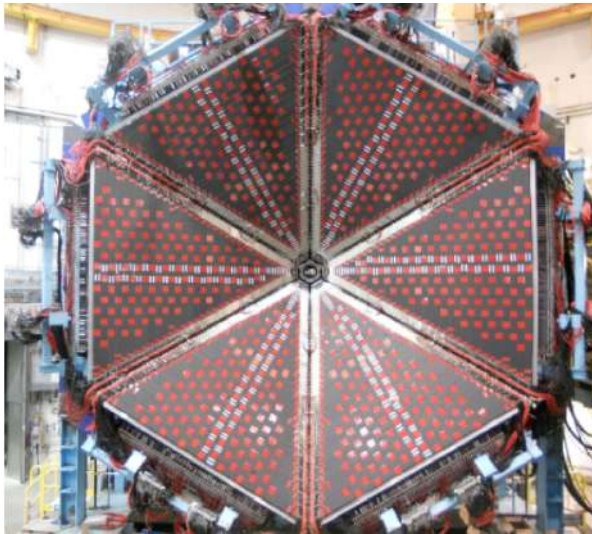


Figure 21: Photograph of the FTOF panel-1b counters mounted on the CLAS12 Forward Carriage in front of the panel-1a counters and the electromagnetic calorimeters before the installation of the panel-2 counters.

the PCAL and the performance of the ECAL, see Ref. [15].

The PCAL and EC are both sampling calorimeters consisting of six modules. Along the direc-

tion from the target, the EC consists of two parts, read out separately, called EC-inner and EC-outer. They provide longitudinal sampling of electromagnetic showers, as well as of hadronic interactions to improve particle identification. Each module has a triangular shape with 54 (15/15/24, PCAL/EC-inner/EC-outer) layers of 1-cm-thick scintillators segmented into 4.5/10-cm (PCAL/EC) wide strips sandwiched between 2.2-mm-thick lead sheets. The total thickness corresponds to approximately 20.5 radiation lengths. Scintillator layers are grouped into three readout views with 5/5/8 PCAL/EC-inner/EC-outer layers per view, providing spatial resolutions of less than 2 cm for energy clusters. The light from each scintillator readout group is routed to the PMTs via flexible optical fibers. Figure 22 shows the PCAL after installation on the Forward Carriage in front of the existing EC from CLAS.

4.8. Forward Tagger (FT)

The Forward Tagger (FT) extends the capabilities of CLAS12 to detect electrons and photons at very forward polar angles in the range from $2.5^\circ \leq \theta \leq 4.5^\circ$. The detection of forward-going scattered electrons allows for electroproduction experiments at very low photon virtuality Q^2 , providing an energy-tagged, linearly polarized, high-intensity, quasi-real photon beam. This configuration enables execution of an extensive hadron spectroscopy program. The FT consists of a calorimeter, a micro-strip gas tracker, and a hodoscope. The electromagnetic calorimeter with 332 lead-tungstate (PbWO_4) crystals is used to identify electrons, measure the electromagnetic shower energy, and provide a fast trigger signal. The tracking system in front of the calorimeter measures the charged particle scattering angles, and the scintillator hodoscope aids in separating electrons and high-energy photons.

Figure 23 shows a photograph of the FT during cosmic ray studies before its installation in CLAS12. During beam operations, a tungsten shielding pipe of conical shape is installed in front of the FT to absorb Møller electrons and low-energy photons produced by beam interactions with the target and downstream materials. This shield protects both the FT and the Forward Detectors from electromagnetic background. The cone angle is 2.5° , compatible with the FT acceptance. In this configuration, known as “FT-ON”, the FT can be used to detect both electrons and photons, extending the detection capabilities of CLAS12. Alternatively, when

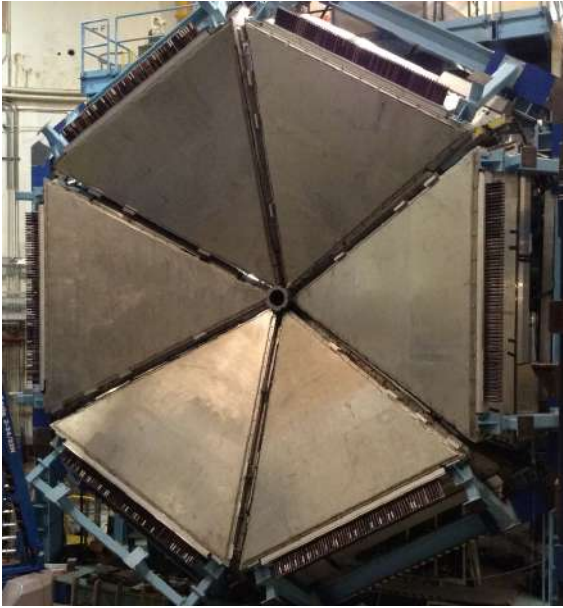


Figure 22: PCAL after installation on the Forward Carriage in front of the existing EC.

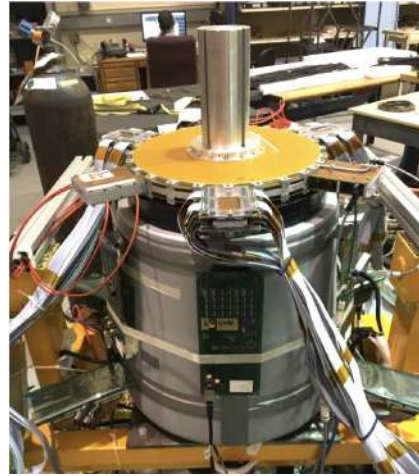


Figure 23: The Forward Tagger system during cosmic ray testing before installation in CLAS12. The lower part contains the electromagnetic calorimeter composed of lead-tungstate crystals. The upper part includes the hodoscope and the tracking disks. Here the FT is rotated by 90° compared to its installation configuration.

549 the FT is not needed for the physics program, the
 550 FT detectors are turned off and additional shielding
 551 elements are installed in front of the FT covering
 552 up to 4.5° to reduce the background in the DC R1
 553 chambers. This configuration, known as “FT-Off”,
 554 reduces the accidental background by one-third at
 555 the same beam conditions, which allows for higher
 556 luminosity data taking with CLAS12. Further details
 557 on the FT are described in Ref. [16]. Figure 24
 558 shows a rendering of the FT setup near the entrance
 559 to the warm bore of the torus magnet.

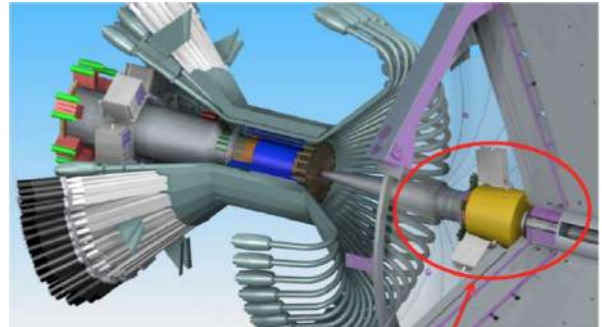


Figure 24: The Forward Tagger system (circled) downstream of the Central Detector in front of the torus magnet warm bore entrance.

5. The CLAS12 Central Detector (CD)

561 Particles scattered from the target at polar angles
 562 in the range from 35° to 125° are detected in
 563 the Central Detector with its own particle identification
 564 and tracking detectors. Charged particles
 565 are tracked in the Central Vertex Tracker (CVT)
 566 and detected in the Central Time-of-Flight (CTOF)
 567 detector with full 360° coverage in azimuthal angle.
 568 Neutron detection is provided by the Central Neutron
 569 Detector (CND) located radially outside of the
 570 CVT and the CTOF. The fully assembled CD is
 571 shown in Fig. 25 after installation in the solenoid.
 572 Figure 26 shows the Central Detector from the up-
 573 stream end.

5.1. Central Vertex Tracker (CVT)

574 The CLAS12 CVT is a part of the Central De-
 575 tector and is used to measure the momentum and
 576 to determine the vertex of charged particles scattered
 577 from the production target, which is centered
 578 within the solenoid magnet. Details of the track-
 579 ing system are shown in Fig. 27. It consists of
 580 two separate detectors, a Silicon Vertex Tracker
 581 (SVT) and a Barrel Micromegas Tracker (BMT).
 582 The SVT system includes 3 regions with 10, 14,
 583 and 18 double-sided modules of silicon sensors in-
 584 strumented with the digital readout ASIC Fermi-
 585 lab Silicon Strip Readout (FSSR2). The readout
 586 pitch is $156 \mu\text{m}$, and the total number of channels
 587

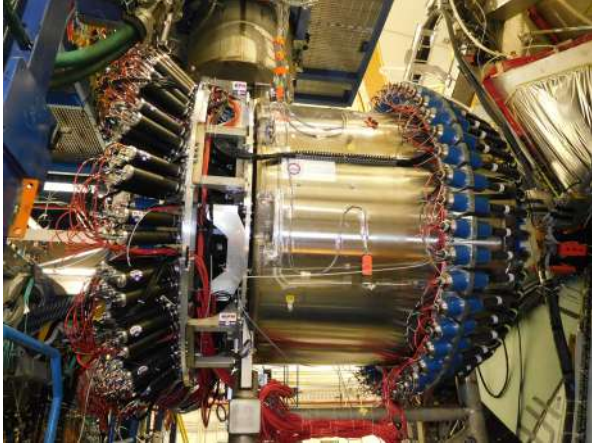


Figure 25: The Central Detector installed in the solenoid magnet in a side view. The readout PMTs are seen at the upstream end (left) and at the downstream end (right) of the solenoid.

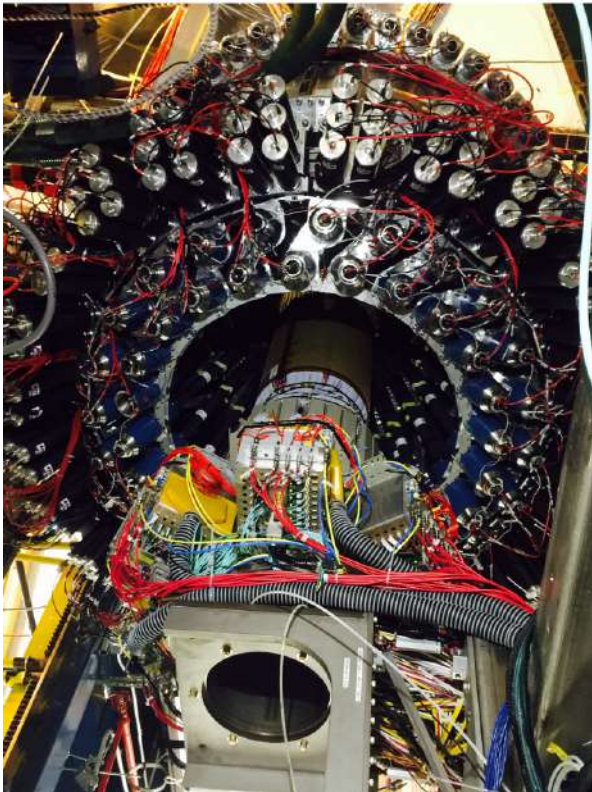


Figure 26: The Central Detector seen from the upstream end. The central tracker system is shown in a retracted position for maintenance. During operation it is fully inserted into the warm bore of the magnet.

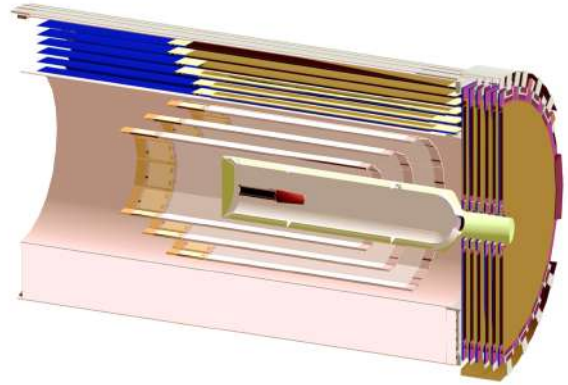


Figure 27: Central Vertex Tracker schematic, showing (from the inside) the target cell and vacuum chamber, the 3 double layers of the SVT, followed by the 6 layers of the BMT. The beam enters from the left. The six FMT layers are shown at the downstream end at the right.

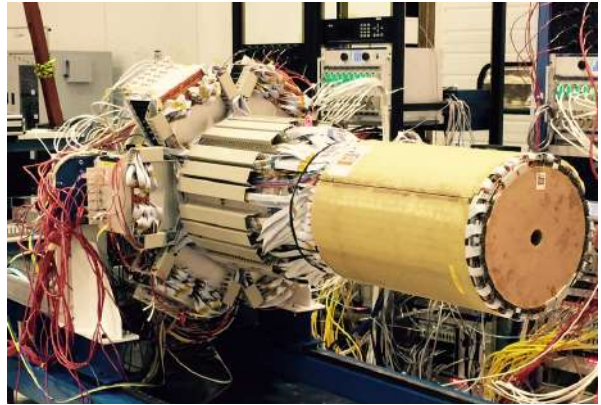


Figure 28: The fully assembled Central Vertex Tracker with the SVT, BMT, and FMT. The BMT and FMT are shown on the outside. The FMT has a circular opening in the center for the electron beam to pass through. The SVT is encapsulated and hidden from view.

588 is 21,504. See Ref. [17] for details on the design,
 589 construction, and performance of the SVT.

590 The BMT contains 3 layers of strips along the
 591 beamline and 3 layers of circular readout strips around
 592 the beamline, with a total number of 15,000 read-
 593 out elements. The BMT provides important im-
 594 provements in momentum resolution and in track-
 595 ing efficiency. Each layer is arranged azimuthally in
 596 3 segments of 120° azimuthal coverage each. The
 597 system operates at the full design luminosity of
 598 $10^{35} \text{ cm}^{-2} \text{ s}^{-1}$.

599 Another component of the CVT is the Forward
 600 Micromegas Tracker (FMT), consisting of 6 lay-

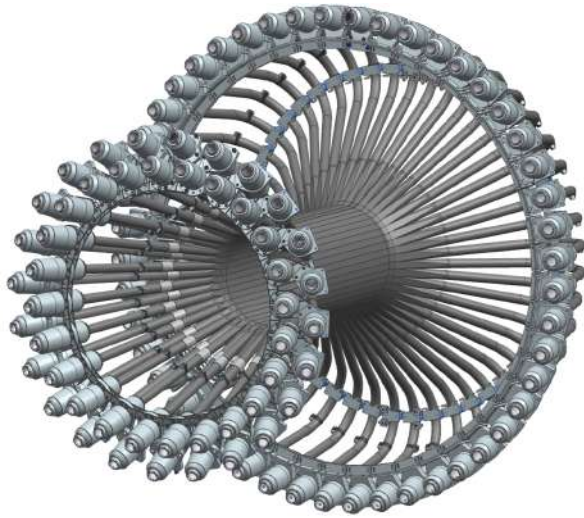


Figure 29: The CTOF detector with its 48 scintillator bars outfitted with light guides, PMTs, and magnetic shields at both ends of each counter.

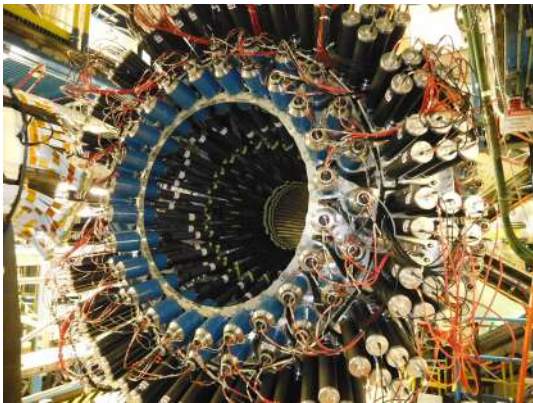


Figure 30: The fully assembled CD as seen from its upstream end with the 144 CND light guides and PMTs at the three outermost rings, and the 48 PMTs of the CTOF (two inner rings).

ers with 6,000 readout elements. It is integrated mechanically with the CVT to provide a compact tracking system, but covers the polar angle range from 5° to 35° and provides improved vertex reconstruction for forward-scattered charged particles. The fully assembled CVT, including the FMT, are shown in Fig. 28. See Ref. [18] for details on the BMT and on the FMT.²

²The FMT was not used during the experimental runs covered in this paper.

5.2. Central Time-of-Flight (CTOF)

The CTOF system is used for the identification of charged particles emerging from the target via time-of-flight measurements in the momentum range from 0.3 to ~ 1.25 GeV. The CTOF includes 48 plastic scintillators with double-sided PMT readout via, respectively, 1.0-m-long upstream and 1.6-m-long downstream focusing light guides. The array of counters forms a hermetic barrel around the target and the CVT. The barrel is aligned with the beam axis inside the 5 T solenoid magnet. The PMTs are placed in a region of 0.1 T fringe field of the solenoid and enclosed within a triple layer dynamical magnetic shield [19] that provides less than 0.2 G internal field near the PMT photocathode. The CTOF system is designed to provide time resolution of 80 ps for charged particle identification in the CLAS12 Central Detector. Details of the CTOF are described in Ref. [20]. Figure 29 shows the CTOF system from the design model and Fig. 30 shows the upstream end of the CTOF installed inside the solenoid.

5.3. Central Neutron Detector (CND)

The CLAS12 CD is also equipped with the CND positioned radially outward of the CTOF that allows the detection of neutrons in the momentum range from 0.2 to 1.0 GeV by measurement of their time-of-flight from the target and the energy deposition in the scintillator layers. The detector is made of three layers of scintillator paddles (48 paddles per layer), coupled two-by-two at the downstream end with semi-circular light guides and read out at the upstream end by PMTs placed outside of the high magnetic field region of the solenoid. The scintillators are connected to 1-m-long bent light guides. Figure 30 shows the upstream readout end of the CND installed in the solenoid. Details of the CND are described in Ref. [21].

5.4. Back Angle Neutron Detector (BAND)

Neutron detection at back angles is accomplished with the BAND, which is positioned 3 m upstream of the CLAS12 target to detect backward neutrons with momenta between 0.25 and 0.7 GeV. It consists of 18 horizontal rows and 5 layers of scintillator bars with PMT readout on each end to measure time-of-flight from the target. There is an additional 1-cm scintillation layer for vetoing charged particles. The detector covers a polar angle range from 155° to 175° with a design neutron detection

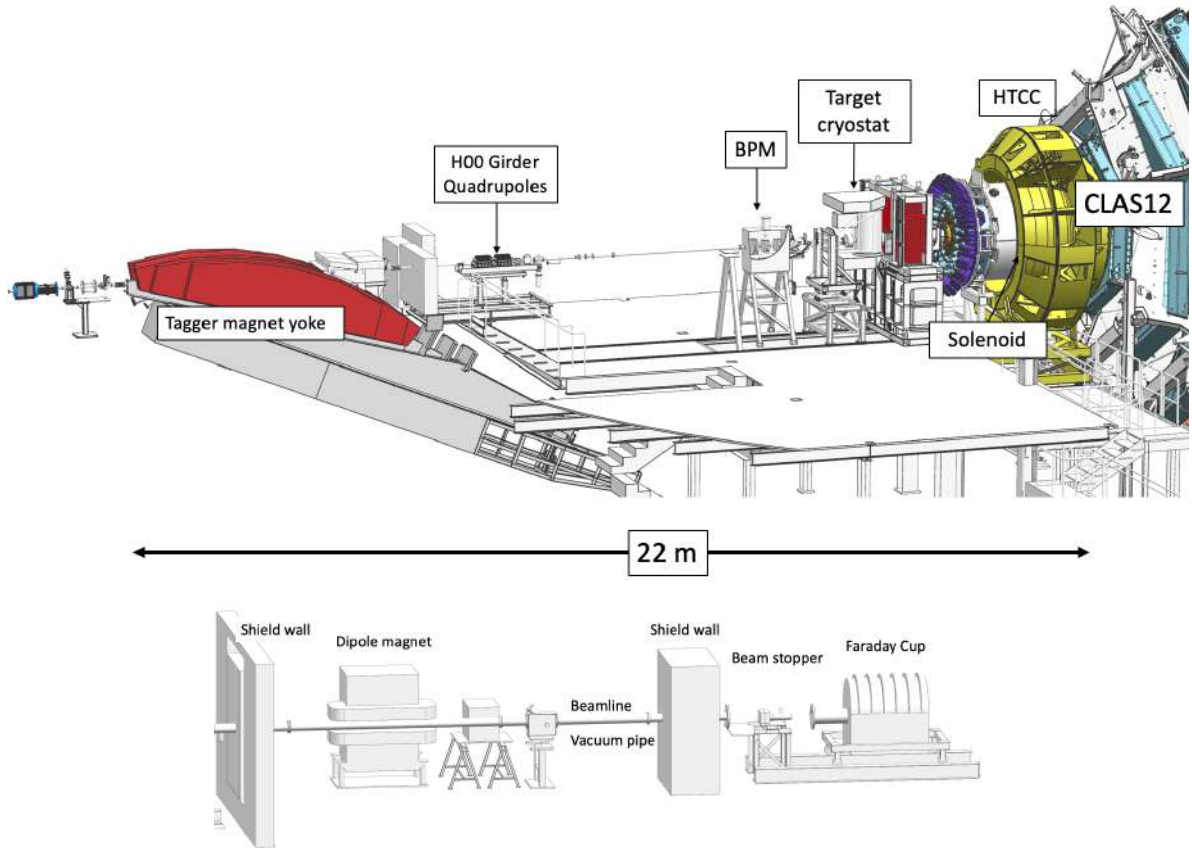


Figure 31: Top: Hall B beamline upstream of the target, showing the tagger magnet (red) to the left, which is energized during beam tuning and during polarization measurements. The doublet seen downstream of the tagger is a pair of quadrupoles. The beam position monitors (BPMs) are used for beam position and beam current measurements. The main element on the right is the solenoid magnet nearly fully encapsulated by the HTCC (yellow). Several of the torus magnet coils are visible at the far right. Bottom: The part of the beamline that extends from the downstream end of CLAS12 to the Faraday cup, a total absorbing device that is used to integrate the beam current to get the total accumulated charge.

658 efficiency of 35% and a momentum resolution of
 659 about 1.5%. Details will be provided in Ref. [22].

660 6. Hall B Beamline

661 The Hall B beamline has two sections, the 2C
 662 line, from the beam switch yard (BSY) to the Hall
 663 proper, and the 2H line, from the upstream end
 664 of the experimental Hall to the beam dump (or
 665 Faraday cup) in the downstream tunnel. Figure 31
 666 shows the portion of the 2H line from the tagger
 667 dump magnet to the entrance to CLAS12 and the
 668 portion of the 2H line downstream of CLAS12 lead-
 669 ing to the Faraday cup.

670 The beamline instrumentation consists of beam
 671 optics, beam position and beam current monitors,

672 beam viewers, collimators, shielding, beam profile
 673 scanners, and beam halo monitors. Devices that
 674 control the beam direction, its profile, and measure
 675 critical parameters, are under the accelerator opera-
 676 tions control. Hall B operators control collimators,
 677 halo monitors, profile scanners, and viewers. They
 678 are also responsible for configuration and running
 679 the Møller polarimeter located upstream of the tag-
 680 ger magnet.

681 The tagger magnet on the left of Fig. 31 (in
 682 red) is not energized during production data taking.
 683 When energized the yoke of this magnet serves as a
 684 beam dump that is used during beam tuning before
 685 the beam is directed on the Hall B production tar-
 686 get. It is also used during specialized runs, such as
 687 polarization measurements in the upstream beam-

688 line, to avoid exposure of sensitive CLAS12 detectors
689 to high background loads. For details of the
690 beamline elements and beam quality, see Ref. [23].

691 The performance of the electron beam and all
692 diagnostic elements in the beamline, status of the
693 beamline vacuum, the superconducting magnets,
694 and the rates in all detector systems that are
695 indicative of potential beam quality issues are directly
696 displayed on a single master screen that is accessible
697 to the shift personnel and other experiment-related
698 personnel and experts. Figure 32 shows the details
699 of the monitoring screen.

700 6.1. Monte Carlo Simulations

701 A critical part of operating an open large-acceptance
702 detector system at high luminosities is the simulation
703 not only of hadronic events but also, and more
704 importantly, the simulation of the beam-related
705 accidental hits in the tracking systems. The source of
706 accidentals is primarily from the beam electron elastically
707 scattering off atomic electrons (Møller electrons)
708 and their secondary interaction with beamline
709 components. The production rate is orders
710 of magnitude larger than the hadronic production
711 rate. These background sources have to be shielded
712 through careful design of magnetic channeling, as
713 well as a proper design and careful optimization
714 of the beamline shielding and the vacuum pipe to
715 minimize interaction of these electrons with high- Z
716 material. The availability of a realistic simulation
717 package was essential for the optimal design of the
718 CLAS12 integrated detector concept.

719 The strong solenoid field is essential in channeling
720 the scattered Møller electrons through the beam
721 enclosure to avoid interactions with the beamline
722 materials. Figure 33 shows a single randomly triggered
723 event at 50% of full luminosity in a time window
724 of 250 ns. This corresponds to the time window
725 in the R1 drift chambers used in the event
726 reconstruction. The main conclusion is that only
727 when both magnets are energized can the detector
728 be operated with acceptable background levels (see
729 Fig. 33 lower left). Additionally, a realistic simulation
730 package is essential for the normalization of
731 cross sections, especially to take into account the
732 detector occupancies for data taking at luminosities
733 near or above the maximum design luminosity
734 where the track reconstruction efficiency can be
735 significantly affected by accidentals. In order to
736 quantitatively account for this, data were taken at
737 different beam currents (i.e. different luminosities)
738 with randomly triggered events. Data from these

739 randomly triggered events were merged with simulated
740 physics events to study the loss of real tracks
741 for different data runs. See Ref. [24] for details on
742 the CLAS12 Geant4 simulation package GEMC.

743 6.2. Experimental Targets

744 Hall B experiments are grouped into running
745 periods with similar beam energy, detector configuration,
746 magnet settings, and target material. The most
747 common target materials have been liquid hydrogen
748 and liquid deuterium. Other materials include
749 solid nuclear targets of various kinds from ^{12}C
750 to ^{208}Pb , depending on the physics requirements.
751 For some specialized experiments high-pressure gas
752 targets are used. All targets are positioned inside
753 CLAS12 using support structures that are inserted
754 from the upstream end, and are independent of the
755 detector itself.

756 A large science program with CLAS12 requires
757 the use of spin-polarized protons and neutrons. Spin-
758 polarized protons and polarized neutrons are used
759 in compound materials where the hydrogen or deuterium
760 can be spin polarized using microwave-induced
761 electron spin transitions in molecules such as in
762 NH_3 and ND_3 . Certain electron spin-flips can be
763 transferred to the proton or neutron in the hydrogen
764 or deuterium atoms, and lead to high polarization
765 of up to 90% for the free protons and over 50%
766 in neutrons of the deuterium atoms in this process
767 of dynamical polarization. To achieve high levels
768 of polarization, a high magnetic field of 5 T is
769 required. In CLAS12, the required magnetic field is
770 externally provided by the 5 T field in the center
771 of the solenoid magnet, which has been designed to
772 provide a homogeneous magnetic field of $\Delta B/B_0 \leq$
773 10^{-3} within a cylindrical region of diameter $\phi =$
774 2.5 cm and $\Delta z = 4$ cm along the beamline. The
775 region near the target cell includes additional
776 correction coils to achieve a factor of 10 better
777 homogeneity that is needed for polarizing the deuterium
778 nuclei in ND_3 . Other polarized materials, such as
779 polarized HD (called HD-Ice), will also be used in
780 support of programs that require spin-polarized
781 targets with the polarization axis oriented transverse
782 to the direction of the electron beam.

783 7. Data Acquisition and Trigger System

784 7.1. CLAS12 Data Flow and Monitoring

785 During data taking the quality of the data is
786 continuously monitored by displaying a very small

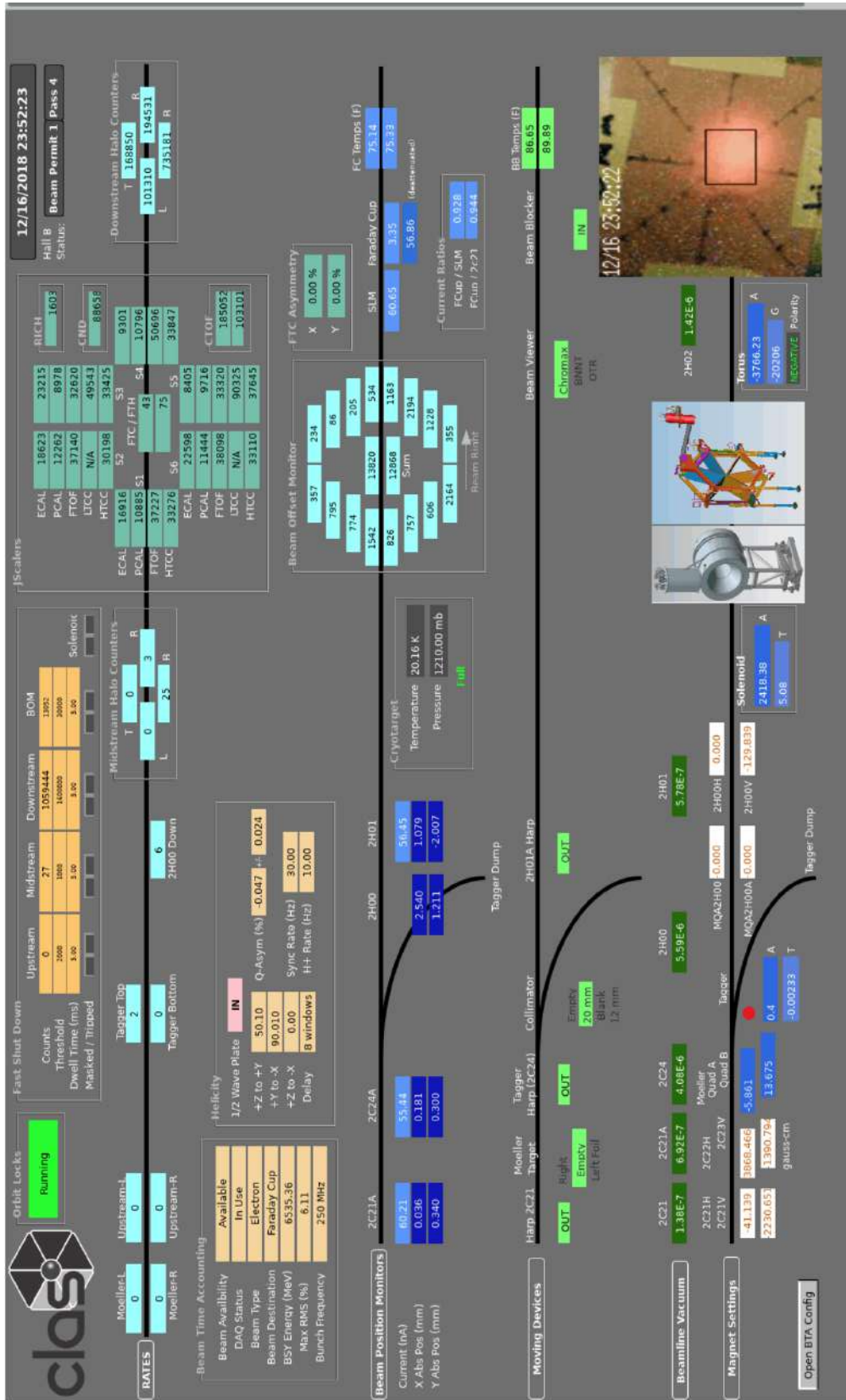


Figure 32: The CLAS12 beamline and detector monitoring systems in Hall B. Top line (left to right) shows the beam halo counters (that typically have zero or single digit rates if the beam quality is good), detector integrated rates in all six sectors, and halo counter rates downstream of the target. Second line: beam position and beam current monitors, status of the cryogenic target, beam offset monitor (16 counters around the beam just upstream of the target), and Faraday cup information. Third line: Devices that can be moved in and out of the beam used for beam viewing and profile measurements, and polarization measurements with Møller scattering. Fourth line: Beamline vacuum conditions, beamline quadrupole settings, CLAS12 torus and solenoid settings, Chromax beam viewer, and beam blocker in front of the Faraday cup.

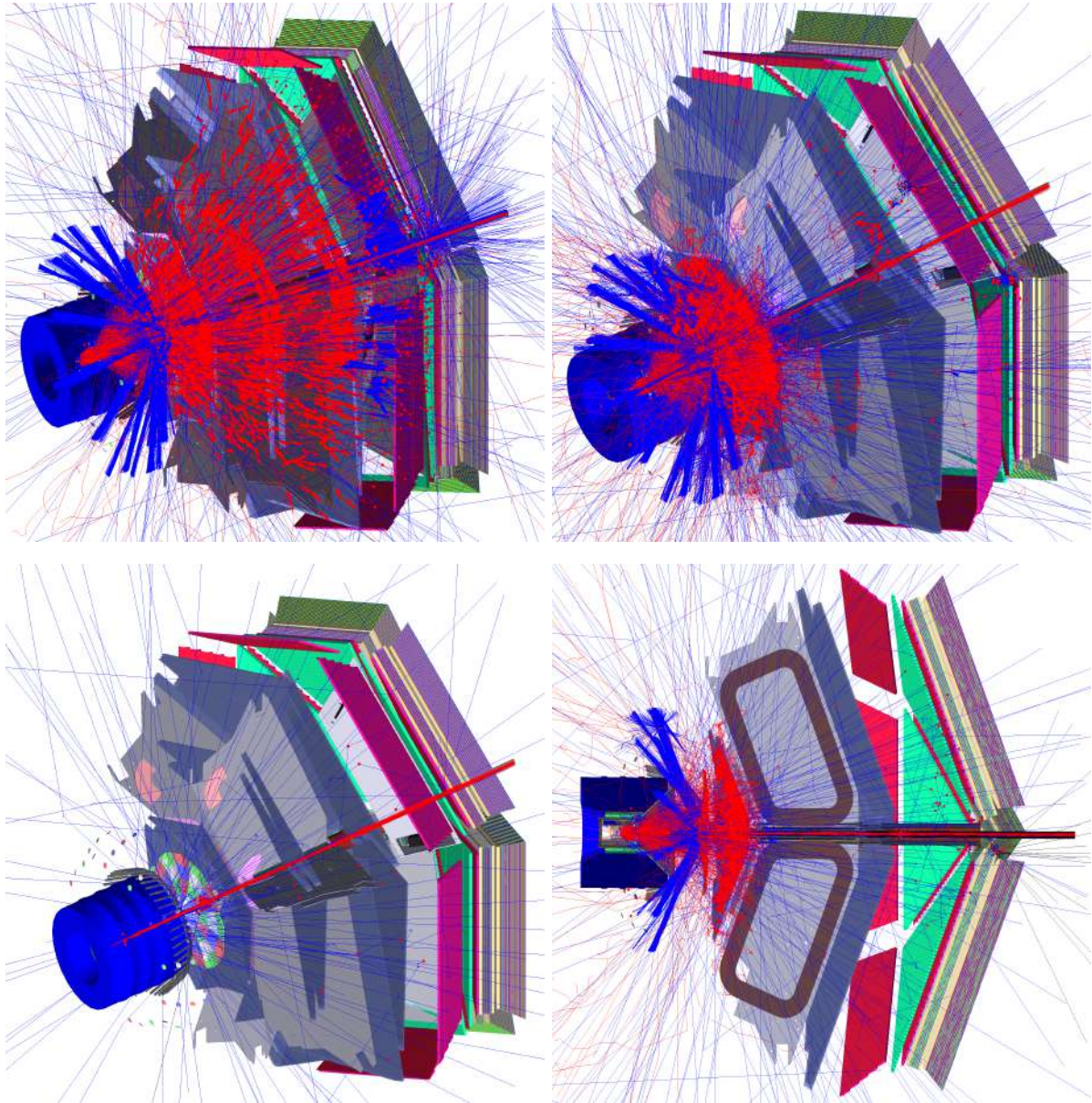


Figure 33: Geant4 representations of accidental background events occurring within a 250 ns time window at different magnetic field configurations and at 50% of design luminosity. Top left: Solenoid field is OFF and torus field is OFF. Top right: Solenoid field is OFF and torus field is ON. Bottom right: Rotated 2D view of top right. Bottom left: Solenoid field is ON and torus field is ON. Color code: red lines are primary electrons; red circles are hits in the detectors; blue lines are photons, including the Cherenkov light, which is clearly visible as the narrow light bundles just at the downstream end of the solenoid magnet, created by the Møller electrons in the HTCC when the solenoid magnet is OFF.

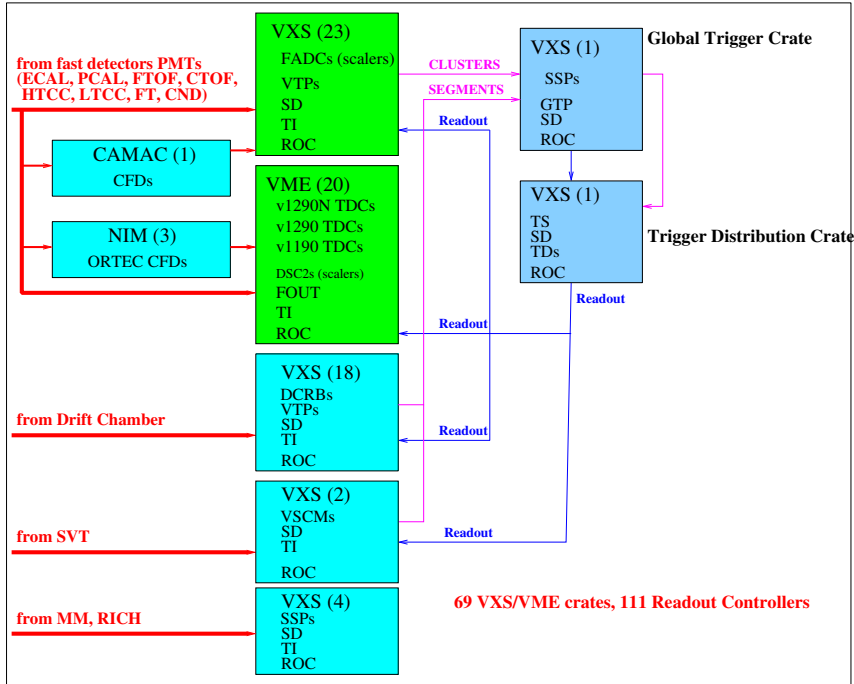


Figure 34: Schematic diagram of the CLAS12 data acquisition and trigger system.

787 fraction of single events in the CLAS12 event display (*ced*) that allows immediate action by the shift
 788 personnel in case of any malfunctioning detector
 789 elements or electronics modules. Monitoring his-
 790 tograms are also filled on a regular basis that in-
 791 clude detector subsystem channel occupancies, as
 792 well as simple analysis plots and can be easily com-
 793 pared with results collected earlier during the data
 794 taking.
 795

796 The CLAS12 data acquisition (DAQ) system is
 797 designed for an average of 20 kHz Level 1 (L1) trig-
 798 ger rate, pipelined for continuous operation. The
 799 sector-based L1 triggers support data streaming,
 800 subsystem hit patterns, and energy summing with
 801 low threshold suppression. The scalable trigger dis-
 802 tribution scheme uses 111 front-end L1 crates. CLAS12
 803 uses different programmable features for each detec-
 804 tor that participates in the L1 trigger. A schematic
 805 diagram showing a complete overview of the DAQ
 806 system is shown in Fig. 34. In 2018 the DAQ was
 807 run at trigger rates of typically 15 kHz and data
 808 rates of up to 500 MB/s with a livetime of >95%.
 809 At somewhat lower livetime of $\sim 90\%$, trigger rates
 810 of 20 kHz and data rates of up to 1 GB/s have been
 811 achieved. Details of the design, functionality, and
 812 performance of the CLAS12 DAQ are provided in
 813 Ref. [25].

814 7.2. Fast and Selective Triggers

815 CLAS12 uses a series of fast triggers that are
 816 tailored to a specific event pattern selection. Most
 817 of the physics experiments require the electron scat-
 818 tered on the production target to be detected as it
 819 defines the mass (Q^2) and kinematics of the virtual
 820 photon as $Q^2 = -(e - e')^2$, where e and e' are the 4-
 821 momentum vectors of the beam electron and of the
 822 scattered electron, respectively. The scattered elec-
 823 tron is uniquely identified with signals in the HTCC
 824 and clustered energy deposition in the ECAL.
 825

826 At the nominal design luminosity of CLAS12,
 827 the hadronic production rate is approximately $5 \times$
 828 $10^6/s$. However, only a small fraction of the events
 829 is of interest for the science program with CLAS12.
 830 In particular, most physics reactions require the
 831 detection of the scattered electrons at some finite
 832 scattering angle, for example $\theta_{e'} > 5^\circ$. Figure 35
 833 shows one example of an electron-triggered event
 834 with one additional positively charged track. The
 835 trigger purity depends on the polarity of the torus
 836 magnet and on the beam-target luminosity. Only
 837 about 50% of the electron triggers recorded with
 838 an inbending torus polarity are actually electrons.
 839 For the outbending torus polarity, the electron trig-
 840 ger purity is as high as 70%. In trigger definition
 list, charged particles in either the FD or the CD

841 can also be selected in the trigger in addition to
 842 the scattered electron making use of the detector
 843 responses.

844 In some experiments the detection of electrons
 845 in the FT is of interest if they are associated with
 846 hadronic event patterns of one or two additional
 847 detected hadrons. Such conditions have been im-
 848 plemented in the fast trigger decision that reduces
 849 the number of triggers to about 2×10^4 events/s, i.e.
 850 by a factor of 250 from the hadronic rate. The data
 851 rate is typically 500 MB/s under such conditions
 852 and can be handled by the CLAS12 data acquisition
 853 system and the available computing resources. Figure 36
 854 shows an example of specific triggers configurations
 855 that have been used during the fall 2018
 856 run period. Details of the design, functionality, and
 857 performance of the CLAS12 trigger system are pro-
 858 vided in Ref. [26].

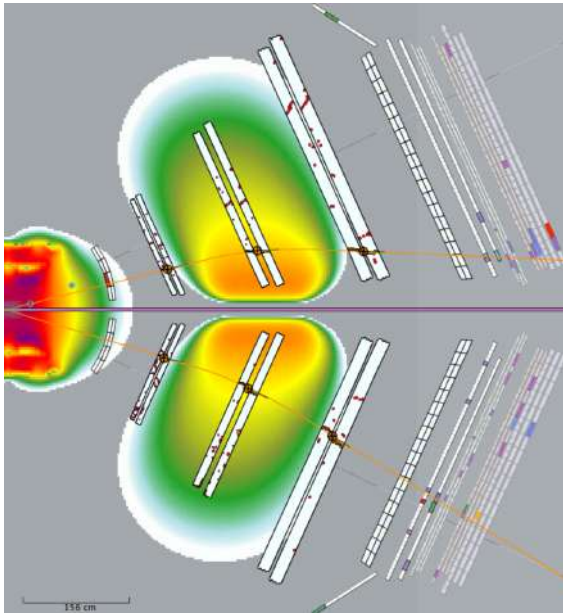


Figure 35: View of an event in CLAS12 from the *ced* event display. Predefined trajectories from a look-up table are employed to select hit patterns in the 3 DC regions that correspond with localized energy deposition in the ECAL. For the two-track trigger, the two sectors show DC hit patterns for tracks with opposite charges. The upper track is an electron, shown by the hit in the HTCC that bends towards the beamline. The lower track has positive charge and bends away from the beamline.

8. CLAS12 Offline Software

The CLAS12 offline event reconstruction is designed to analyze large amounts of beam-induced



Figure 36: The CLAS12 trigger control screen during a specific data run with a total of 17 active triggers operating at a livetime of 95.4%. Nearly half (48.7%) of all triggers are from single electrons detected in one of the 6 FD sectors. Over a quarter (27.81%) of all triggers required an electron in the FT with an additional two charged hits detected in the FTOF and in the PCAL. Several others were taking data at the 5% level and required charged tracks in the FTOF and ECAL in opposite FD sectors. Finally, several other triggers were used for monitoring purposes and were heavily pre-scaled.

862 experimental data acquired during production and
 863 cosmic ray runs; the latter being used for alignment
 864 and calibration purposes. The CLAS12 reconstruction
 865 framework is built based on a service-oriented
 866 software architecture, where the reconstruction of
 867 events is separated into micro-services that execute
 868 data processing algorithms. The software packages
 869 consist of the event reconstruction, visualization,
 870 and calibration monitoring services, as well as de-
 871 tector and event simulations.

872 During the CLAS12 design phase a realistic sim-
 873 ulation package based on Geant4 was developed to
 874 aid in the optimization of the detector hardware re-
 875 sponse to beam interactions in terms of resolution,
 876 robustness of operation at high luminosity, details
 877 of the beamline design, and other aspects.

8.1. Event Reconstruction

879 Event reconstruction in the CLAS12 FD con-
 880 sists of the identification of charged and neutral

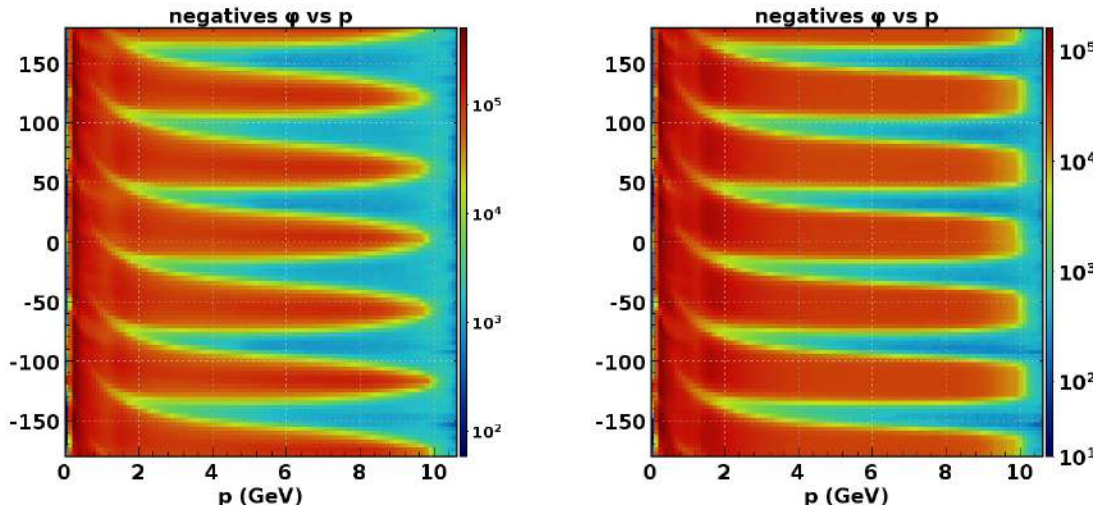


Figure 37: Particle distributions in azimuthal angle (ϕ) vs. momentum in the CLAS12 FD for inbending electrons (left) and with reversed torus field for outbending electrons (right) at a beam energy of 10.6 GeV. The azimuthal angle is measured at the production vertex. The azimuthal distribution of inbending electrons narrows with increasing momentum, as high-momentum electrons in CLAS12 are bent towards the beamline, where detector acceptances are reduced. This is not the case for outbending electrons that are deflected away from the beamline toward larger detector acceptances. The $p - \phi$ correlation, most visible at low momentum, is due to the solenoidal magnetic field that bends charged tracks dependent on their transverse momentum component and on their charge. For positively charged tracks the ϕ motion is in the opposite direction from negative (electron) tracks. Color axes indicate the particle yields.

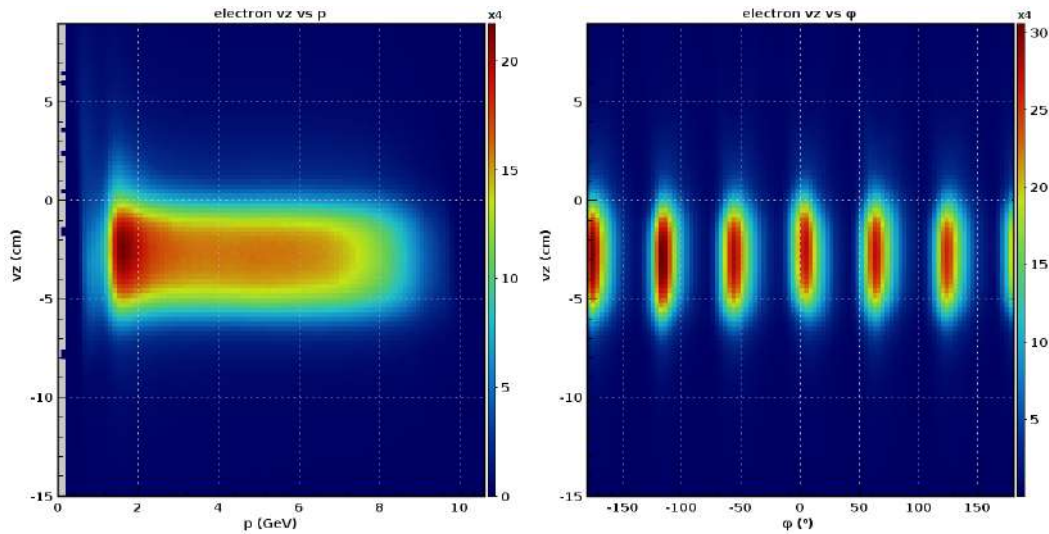


Figure 38: Reconstructed vertex along the beamline vz for electrons in the FD. Left: vz vs. momentum, Right: vz vs. azimuthal angle. The vertical size of the vertex band is consistent with the target length of 5.0 cm.

881 particles along with the determination of their 3-
 882 momenta and reaction vertex at the distance of
 883 closest approach to the beamline. Charged particle
 884 reconstruction requires both forward tracking and
 885 FTOF information.

886 Track reconstruction in the FD is based on a hit

887 clustering algorithm that requires at least 4 out of 6
 888 connected DC cells to form a track segment within
 889 each superlayer. The tracking algorithm requires
 890 at least 5 out of 6 superlayers in a sector to form
 891 a track candidate. The first stage of tracking relies
 892 solely on the DC wire positions to fit the tracks and

to provide matching to the outer detectors subsequently required to obtain timing information. At the second stage of tracking, timing information is used to determine a time-based track and the particle momentum and flight path, while the FTOF gives the particle velocity (β) when combined with flight-path information (see Ref. [27] for details). The momentum and velocity information are combined to give the particle mass: $m = p/\beta\gamma$. Electron identification additionally requires the track to match in time and position with both an HTCC hit and an isolated shower in the ECAL. The energy of the shower must be consistent with the track momentum measured by the DCs in the torus magnetic field.

Charged particles are tracked in each sector separately using the 3 regions of DCs in each sector. Most tracks are confined within one sector as the magnet optics and the massive mechanical support of the torus coils prevent most tracks from crossing from one sector into a neighboring sector. In rare cases low-momentum charged pions can cross from one sector into the opposite sector traversing through the beam pipe. Such tracks are not reconstructed but they are included in the event simulation. Distributions of charged particles in azimuthal angle vs. momentum are shown in Fig. 37. Figure 38 shows the production vertex as reconstructed in the FD tracking system (from data where the FMT was not installed). As the tracking detectors in each sector are independent of each other, they have to be independently aligned and calibrated. The reconstructed vertex is independent of the sector and also independent of the electron momentum, is an indication that the tracking detectors are well aligned.

Neutral particles are detected in either the calorimeters or in the FTOF (or both). The reconstruction begins by finding isolated clusters of energy, and determining the spatial location, deposited energy, and the time of the cluster. Neutral particle candidates are identified as clusters in the outer detectors (FTOF, PCAL, EC) that do not match any charged particle track. For high-energy photons that deposit all of their energy in the calorimeters, the energy is calculated from the signal pulse height in the calorimeters. The momenta of neutrons are computed from their flight time as determined by the timing signal in the calorimeters and, when relevant, the matched FTOF counter. In either case, the angle of the neutral particle trajectory is determined from the position of the cluster at a depth

in the ECAL that minimizes parallax effects associated with tracks that are not normal to the face of the ECAL (see Ref. [15] for details).

For all events, precise determination of the interaction time or event start time is required. For events where the scattered electron is detected, the event start time is derived from the arrival time of the electron at the FTOF counters, corrected for flight path and signal delays. The average time resolution for electrons reconstructed in the CLAS12 FD is better than 80 ps. A more accurate event start time is obtained by replacing the measured electron start time with the 499 MHz accelerator RF signal (or 249.5 MHz depending on the accelerator setup) that determines the beam bunch associated with the event. In this way, the event start time can be determined to within ~ 20 ps, thus eliminating a significant contribution to the time resolution smearing for charged hadrons. This extends the charged particle identification capabilities of CLAS12 towards higher particle momentum.

Track reconstruction in the CD is generally less complex as tracks are determined fully by the geometry of the detection elements and the hit pattern in the CVT, i.e. by a combination of the SVT and the BMT trackers. In contrast to the charged particle tracking in the FD that relies heavily on timing information for resolution, this is not the case for the CD. In principle, that makes tracking easier in the CD. On the other hand, the redundancy of track fitting is much reduced in the CD as there are only 12 tracking layers compared to the 36 in the FD. This makes tracking in the CD more susceptible to losing tracks due to accidental hits. Charged particle identification in the CD is given by the timing information in the CTOF (or CND) scintillators combined with the track momentum measured in the strong solenoid magnetic field.

Neutral particles are detected in the CD in the CND or the CTOF (or both). As for the FD, neutral particle candidates are identified as clusters that do not match any charged particle track. See Ref. [27] for full details on the CLAS12 offline reconstruction software architecture and design.

9. CLAS12 Operational Performance

This section describes the overall performance of the CLAS12 detection system. Most of the experimental programs require the clean identification and reconstruction of the scattered electron. Electrons are identified by a combination of signals in

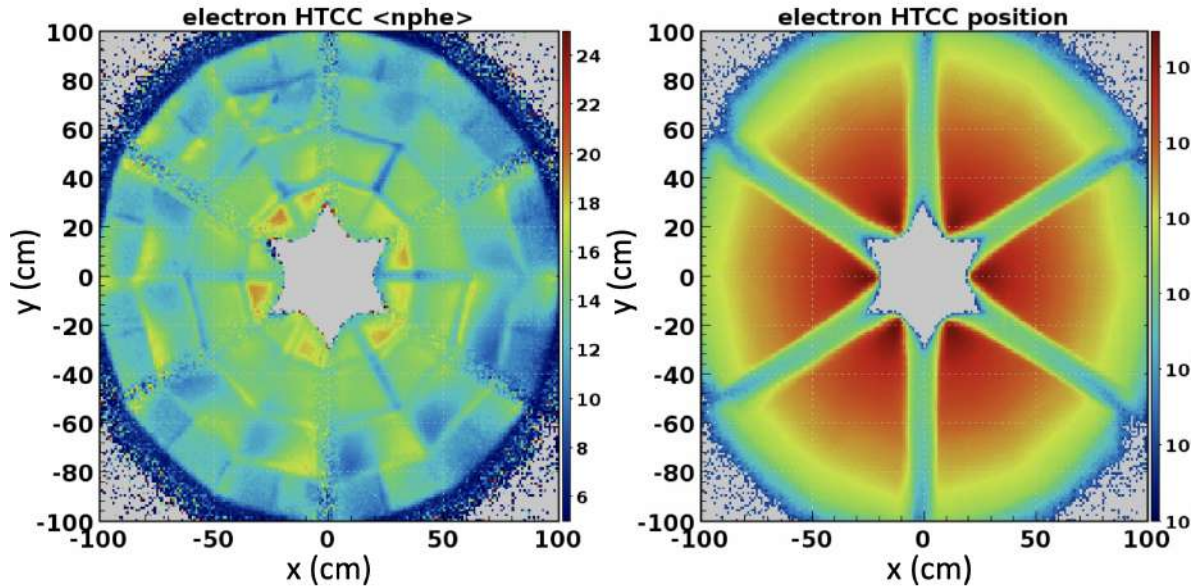


Figure 39: Distribution map of the number of photoelectrons collected in polar and azimuthal angle of the HTCC shown in terms of the y vs. x transverse coordinates. The plot is based on measurements with a trigger threshold of 2 photoelectrons. The averaged electron detection efficiency is estimated at greater than 99% in the full phase space covered by the HTCC. In localized areas, in particular at interfaces of different mirror facets or between mirror sectors, the efficiencies can be as low as 94%. This map enables bin-by-bin corrections for absolute normalization. Right panel: Distribution of electrons from forward tracking reconstruction at the HTCC location in polar and azimuthal angle. The gaps between sectors are due the scattered electrons being lost in the torus coils and not reconstructed.

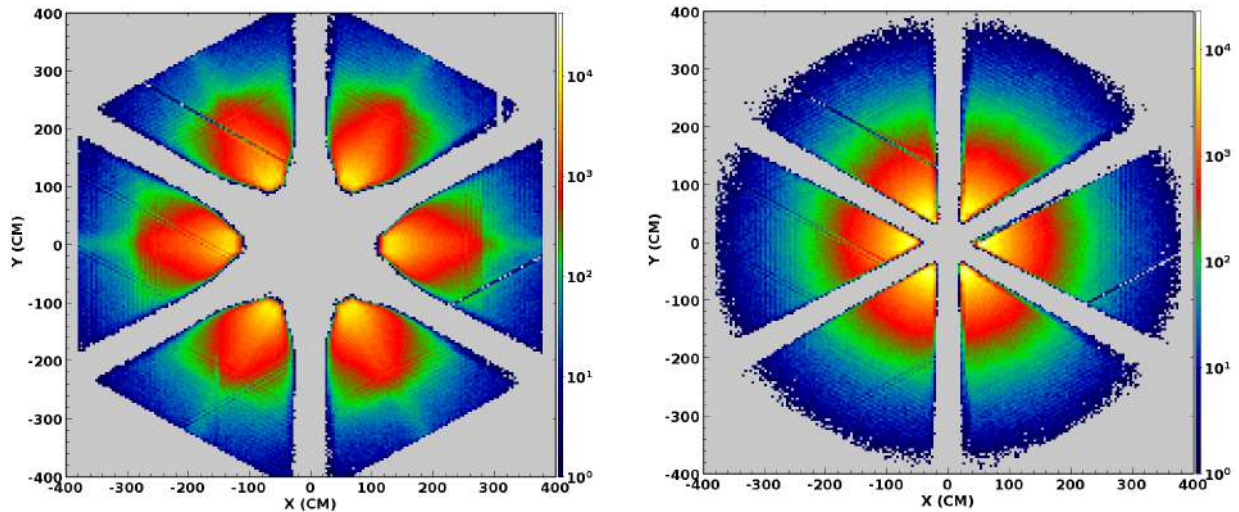


Figure 40: Distribution of electron track y vs. x coordinates propagated to the PCAL front face (as seen from the target). The few empty strips are due to hardware issues. (Left) Data for electrons bent away from the beamline (outbending). Right: Data for electrons bent toward the beamline (inbending).

995 the HTCC and energy deposited in the combined
 996 electromagnetic calorimeters PCAL and EC, with a
 997 matched negatively charged track in the DC track-
 998 ing system. Of critical importance is the response

999 of the HTCC that operates between the CD and
 1000 the entrance to the DC system. The reconstructed
 1001 electron coordinates at the HTCC are shown in
 1002 Fig. 39(right), exhibiting a very uniform distribu-

tion in azimuthal angle. The distribution of photoelectrons across the entire 48 segments of the HTCC active region is shown in Fig. 39(left), which exhibits a rather uniform and high efficiency for electrons over its full acceptance.

The coordinates of the reconstructed electrons at the front face of the PCAL are shown in Fig. 40 for electrons bending towards the beamline, and with reversed torus magnetic field with electrons bending away from the beamline. The different appearance of the two plots is the result of the difference in optics for the two configurations. The distributions are rather uniform in all six sectors, showing that the detector systems and the reconstruction software are working properly. The few empty strips indicate malfunctioning detector elements or electronics modules. The acceptances for the inbending and the outbending scattered electron show quite different features. Outbending electrons hit the ECAL front face significantly further out radially than inbending electrons do. This is a feature of the magnetic field of the torus magnet. Also, the outer acceptance bounds are quite different. In the outbending case, they are defined by the ECAL geometry, while for the inbending case the acceptance bounds are given by the HTCC geometry, as can be seen in Fig. 39.

Elastic scattering of electrons on protons allows for the establishment of any deviations from the ideal detector geometry and alignment. The coverage in kinematical quantities Q^2 and x_B of the scattered electrons detected in the FD is shown in Fig. 41. Q^2 is the virtuality of the photon exchanged from the electron to the proton target and x_B is the Bjorken scaling variable (defined as $Q^2/(2ME_\gamma)$ where M is the target mass and E_γ is the energy of the virtual photon exchanged with the target). The electron kinematics also define the invariant mass W defined as $W^2 = M^2 + 2M\nu - Q^2$, with $\nu = E_e - E_{e'}$ and M the mass of the target particle. For inbending electrons the coverage in Q^2 is up to 13 GeV^2 at $x_B \approx 1$, while for the outbending electrons it is limited to $Q^2 \approx 12 \text{ GeV}^2$.

9.1. Charged Particle Detection in the FD

Charged particle yields in momentum and azimuthal angles are shown in Fig. 37 in the local sector frame for positively and negatively charged particles. The difference in the acceptance is due to two factors, the polarity of the torus magnet that bends negative particles away from the beamline and positive particles towards the beamline (or

vice-versa for the opposite torus polarity), and the effects of the solenoid magnetic field that causes an azimuthal motion for positive and negative particles in opposite directions.

Identification of charged particles in CLAS12 is achieved in a number of ways. Identified electrons are used to determine the hadron start time at the production vertex. The start time and the path length of charged tracks from the production vertex to the FTOF and the FTOF hit time, enable the determination of the velocity ($\beta = v/c$) of the particle, shown in Fig. 42 vs. particle momentum for positively charged tracks. The computed mass squared vs. momentum for these tracks is shown in Fig. 43. An overview of the detector subsystems in the CLAS12 FD used for the identification of the different charged particle species vs. momentum is shown in Fig. 44.

Figure 45 shows the inclusive invariant mass W spectra for $ep \rightarrow e'X$ and missing mass spectra for $ep \rightarrow e'\pi^+X$ with a missing neutron at four different beam energies. Figure 46 shows the invariant mass of $\pi^+\pi^-$.

9.2. Charged Particle Detection in the CD

Momentum reconstruction in the CVT combined with the timing information from the CTOF allows for the separation of charged pions, kaons, and protons in the momentum range from 0.3 GeV to 1.25 GeV. This momentum range covers a large part of the phase space allowed by the maximum beam energy for hadron electroproduction on hydrogen targets. Figure 47 shows the reconstructed mass squared vs. particle momentum reconstructed in the CVT.

9.3. Neutral Particle Detection

Direct detection of neutral particles is accomplished in the FD using the PCAL and EC calorimeters. The combined 20 radiation lengths are sufficient to identify high-energy photons and reconstruct the masses of the parent particles, such as $\pi^0 \rightarrow \gamma\gamma$ or $\eta \rightarrow \gamma\gamma$. At very forward angles the FT provides photon detection with significantly improved position and energy resolution in the polar angle range from 2.5° to 4.5° . Figure 48 shows the invariant mass of the $\gamma\gamma$ system in the CLAS12 FD. The energy response of the FT to 2.2 GeV electrons and the $\gamma\gamma$ mass resolution are shown in Fig. 49.

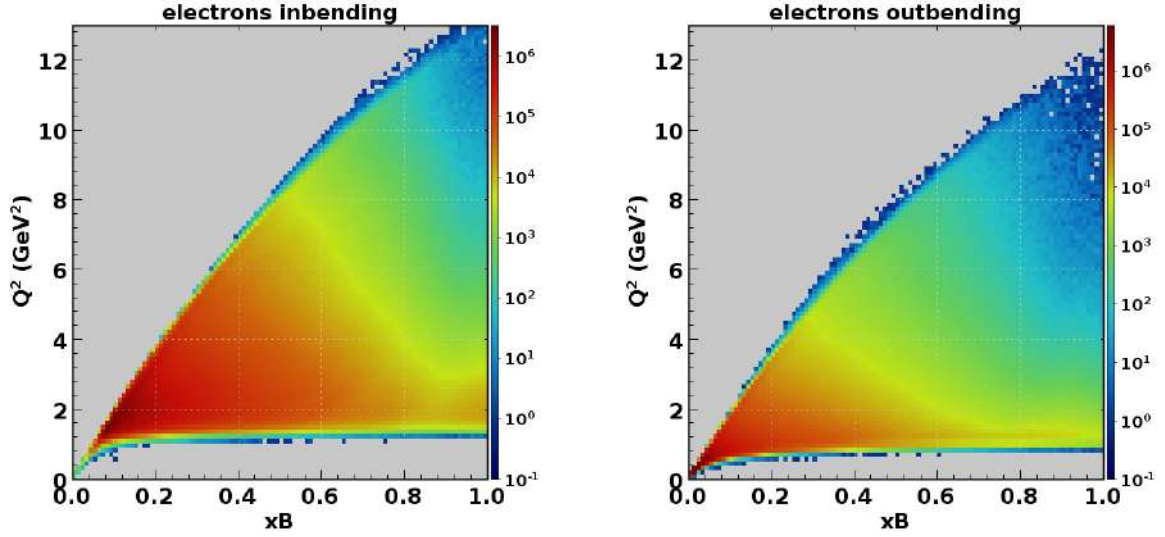


Figure 41: Inclusive $ep \rightarrow e'X$ coverage in Q^2 vs. x_B at a beam energy of 10.6 GeV. The full kinematics is measured simultaneously. The kinematic range is given by elastic scattering kinematics at $x_B = 1$, and the small angle acceptance at the Q^2 limit for scattered electrons bending (left) toward the beamline (inbending) or (right) away from the beamline (outbending). The two configurations require opposite directions of currents in the torus magnet coils. Note that the minimal Q^2 is lower for the electron outbending configuration, and that the maximum Q^2 reach is slightly higher for inbending electrons.

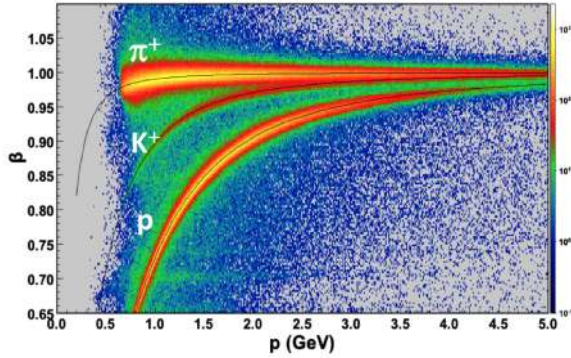


Figure 42: $\beta = v/c$ vs. momentum of positively charged particles detected in the CLAS12 FD. Events were selected to have an electron identified. The charged particle trajectories are reconstructed and their path length and timing from the target to the FTOF (panel-1b layer) are determined. The start time at the target is given by identifying the corresponding beam bucket as time $t=0$. The thin black lines show the expected distributions for the respective charged tracks. Particle identification is limited to momenta greater than 0.8 GeV when the torus magnet is energized to maximum current. At reduced torus current the tracking is extended to lower momenta at the expense of momentum resolution.

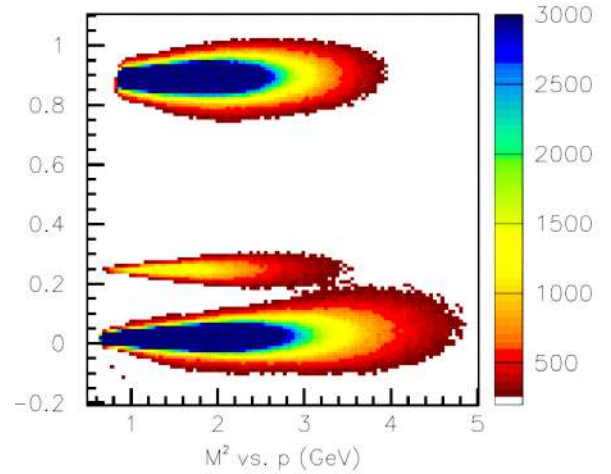


Figure 43: Reconstructed mass squared vs. momentum of positively charged particles in the CLAS12 FD. The same data are used as in Fig. 42. However, the plot contains a threshold on the minimum and maximum number of events per bin to eliminate background events between the particle bands, and to better visualize the scarce kaons in the particle samples, which are of special significance for the science program. Bottom: π^+ , middle: K^+ , top: p . The centroids of each particle distribution are approximately independent of the momentum. Masses are computed from the particle path length and from time-of-flight. Any momentum dependence would indicate systematics in the timing calibration or in the path length determination.

1101 Neutral particle detection in the CD is provided
 1102 by the CND combined with the CTOF. The plas-
 1103 tic scintillator bars of the CND have an $\approx 12\%$ nu-
 1104 clear interaction length, resulting in a $\approx 10\%$ ef-

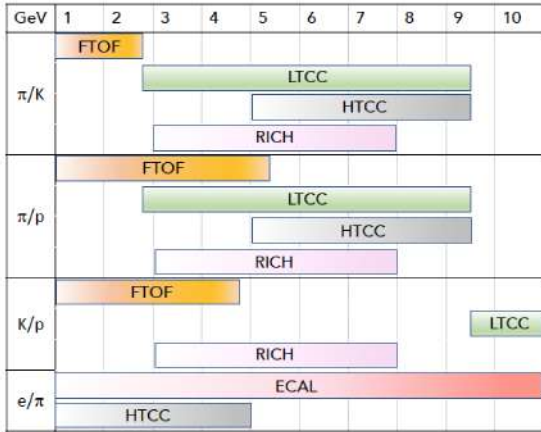


Figure 44: Overview of the different detector subsystems in the CLAS12 FD used for particle species separation vs. momentum.

1105 efficiency for the detection of high-energy neutrons. 1153
 1106 The plastic scintillators contribute about 29.6% of 1154
 1107 a radiation length at $\theta=90^\circ$; hence they also de- 1155
 1108 tect high-energy photons through their conversion 1156
 1109 into e^+e^- pairs. The discrimination of photons and 1157
 1110 neutrons in the CD is accomplished by the timing 1158
 1111 resolution of 80 to 100 ps provided by the CTOF 1159
 1112 and the 160 ps of the CND. The separation of neu- 1160
 1113 tral particles from charged particle hits in the CND 1161
 1114 or in the CTOF is efficiently achieved by using the 1162
 1115 CVT tracker to veto against false neutral hits in the 1163
 1116 CTOF and CND. Figure 50 shows the velocity vs. 1164
 1117 the energy deposition of charged and neutral parti- 1165
 1118 cles in the CND. The measured neutron detection 1166
 1119 efficiency is shown in Fig. 51.

1120 At far backward angles, the BAND detector pro- 1167
 1121 vides neutron identification with detection efficien- 1168
 1122 cies up to 35%. As there are no tracking capabili- 1169
 1123 ties in the very backward direction, the separation 1170
 1124 of charged particles is achieved by a veto counter, 1171
 1125 corresponding to a 1-cm-thick scintillation counter 1172
 1126 in front of the BAND. The separation of neutrons 1173
 1127 and photons is achieved by the timing information, 1174
 1128 which is shown in Fig. 52.

10. Electron Beam Operation

1129 During beam operation the status of the beam- 1179
 1130 line diagnostics and other critical components, as 1180
 1131 well as most of the detector components, are contin- 1181
 1132 uously monitored. Some of the beamline elements 1182
 1133 are used to warn of beam conditions that may neg- 1183

1135 atively impact detector operation and are used as
 1136 a fast shutdown of beam delivery.

10.1. Forward Detector Reconstruction

1137 The science program with CLAS12 in general re- 1138
 1139 quires the detection of electrons that are scattered 1139
 1140 off the target material. For determining the kine- 1140
 1141 matics of the reaction, the electrons must be iden- 1141
 1142 tified and their 3-momentum determined by track- 1142
 1143 ing them in the magnetic field of the torus mag- 1143
 1144 net, and detecting them in the FTOF and in the 1144
 1145 ECAL, which covers approximately the polar an- 1145
 1146 gle range from 5° to 35° . The detailed acceptance 1146
 1147 ranges depend also on the polarity of the torus mag- 1147
 1148 netic field. Charged tracks that are deflected away 1148
 1149 from the beamline have acceptance functions that 1149
 1150 are different from charged tracks that are deflected 1150
 1151 toward the beamline. Figure 53 shows the distribu- 1151
 1152 tion of reconstructed electrons vs. azimuthal angle 1152
 ϕ for different ranges of polar angle θ at 8° and 26° 1153
 1154 showing the different acceptances for outbending 1154
 1155 vs. inbending electrons.

1156 The magnetic field of the solenoid also affects 1156
 1157 the acceptance function of charged particles. For 1157
 1158 opposite charges but the same momentum, the az- 1158
 1159 imuthal rotation of scattered charged particles is 1159
 1160 the same in magnitude but opposite in sign. The 1160
 1161 particle acceptance is a complex function of the 1161
 1162 phase space covered by the processes of interest and 1162
 1163 must be simulated in full detail to precisely extract 1163
 1164 cross sections and other physics observables. For 1164
 1165 this purpose a full simulation package was devel- 1165
 1166 oped, based on the software package Geant4 [24].

10.1.1. Luminosity Performance During CLAS12 Operations

1167 CLAS12 is designed for operation at a luminos- 1167
 1168 ity of $L = 10^{35} \text{ cm}^{-2}\text{s}^{-1}$, which corresponds to a 1168
 1169 beam current of 75 nA and a liquid-hydrogen target 1169
 1170 of 5 cm length. The high-luminosity operation has 1170
 1171 measurable effects on the hit occupancy in the drift 1171
 1172 chambers and on the resolution in the reconstruction 1172
 1173 of kinematical quantities. Also, the reconstruction 1173
 1174 efficiency of charged particles can be affected. 1174
 1175 Figures 54 and 55 show the hit occupancies in the 1175
 1176 drift chambers for different beam currents and for 1176
 1177 different currents in the solenoid magnet, respec- 1177
 1178 tively.

1179 The effects of luminosity on the reconstruction 1179
 1180 can be studied in simulations when the beam con- 1180
 1181 ditions can be realistically imposed on the data. 1181
 1182
 1183

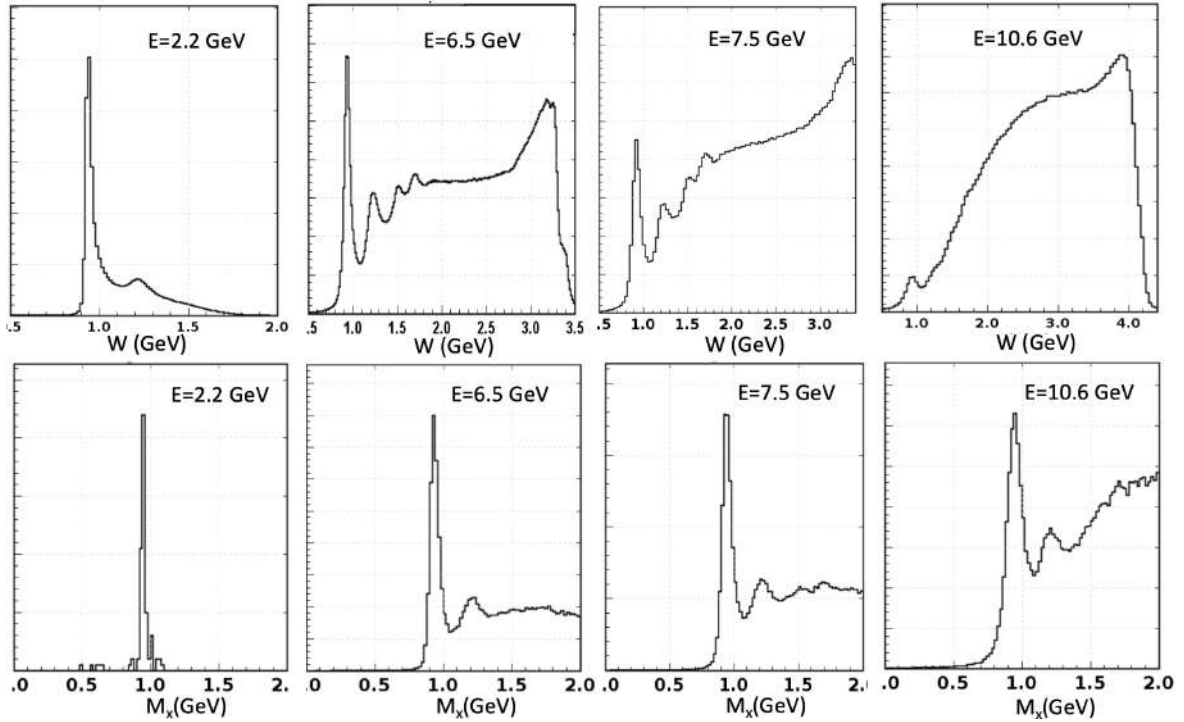


Figure 45: Upper row: Inclusive electron scattering spectrum $ep \rightarrow e'X$ measured in CLAS12 at beam energies of 2.2 GeV, 6.5 GeV, 7.5 GeV, and at 10.6 GeV (from left to right). The peak to the left is due to elastic $ep \rightarrow ep$ scattering. Enhancements from the first 3 excited nucleon states, $\Delta(1232)$, $N(1520)$, and $N(1680)$, are also visible for the lower beam energies. Note that the mass ranges are different for the different beam energies. Lower row: Missing mass distributions of $ep \rightarrow e'\pi^+X$ for the same energies. The sharp mass peak to the left is due to the undetected neutron. The second peak for the higher energies is due to the $\Delta^0(1232)$. Indications of higher mass neutron excitations are also visible.

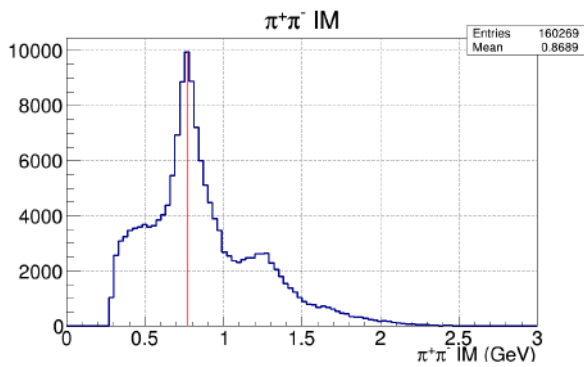


Figure 46: Invariant mass of $\pi^+\pi^-$ at 10.6 GeV beam energy. The vertical line indicates the mass of the $\rho^0(770)$ meson. The shoulder to the right is from the $f_2(1270)$ meson.

1184 For that purpose a procedure was developed that
 1185 takes randomly triggered events at the operating
 1186 beam current and superimposes these events on the
 1187 simulated events without the background. In this
 1188 way one can study the reconstruction efficiencies

1189 as a function of luminosity of the actual experi-
 1190 ment. With increasing luminosity, accidental out-
 1191 of-time events can affect and alter particle tracks
 1192 that come in-time. The most important effect is
 1193 that the track quality is negatively impacted, lead-
 1194 ing to track losses if stringent quality requirements
 1195 are applied, or to a worsening of the angle and mo-
 1196 mentum resolution. This effect is demonstrated in
 1197 Table 1.

1198 Another way of quantifying the effect of acci-
 1199 dental background is by studying the percentage of
 1200 tracks lost when certain track quality requirements
 1201 are imposed. Detailed simulations must be done for
 1202 specific operating conditions, such as magnetic field
 1203 settings, event triggers, beam current, and produc-
 1204 tion targets. As an illustration, an example of such
 1205 a simulation is shown in Fig. 56. The process simu-
 1206 lated was elastic muon-proton scattering (which,
 1207 of course is not feasible at an electron accelerator),
 1208 where the proton mass is inferred from the elastic
 1209 muon track, and compared with the known proton

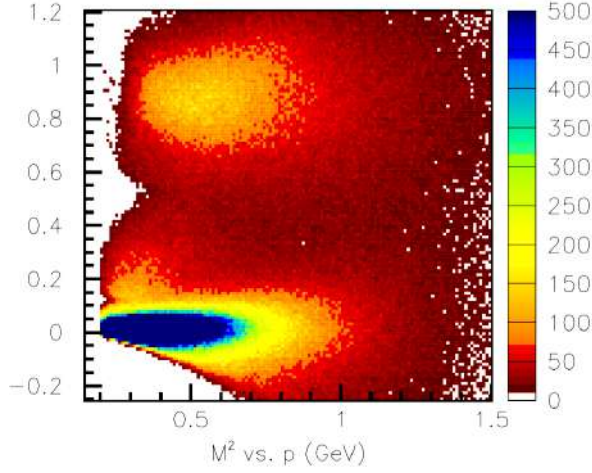


Figure 47: Mass squared of positively charged particles evaluated from their path length and the time-of-flight information in the CTOF vs. the particle momentum at 10.6 GeV beam energy. The band at the bottom is from π^+ , the faint band near 0.2 is from K^+ , and the band at the top is from protons. The momenta are not corrected for energy loss in the CVT.

Parameter	Current	Resolution	Specs
$\Delta p/p$ (%)	0 nA	0.52	≤ 1
	60 nA	0.67	
	120 nA	0.86	
$\Delta\phi$ (mrad)	0 nA	3.3	≤ 4.5
	60 nA	3.8	
	120 nA	4.4	
$\Delta\theta$ (mrad)	0 nA	0.66	≤ 1
	60 nA	0.85	
	120 nA	0.85	
Δv_z (mm)	0 nA	3.5	-
	60 nA	4.6	
	120 nA	5.6	

Table 1: Impact of high-current operation on the resolution of kinematic quantities in single track reconstruction. The resolution parameters are without the use of the FMT tracker, which should significantly improve the v_z -vertex resolution. Note that the highest beam current of 120 nA is 60% higher than the nominal operating value of 75 nA.

1210 mass. Muons were used as an ideal probe that does
 1211 not require corrections for radiative effects as elec-
 1212 tron scattering does. At higher beam currents, in-
 1213 creasingly wider tails develop on the inferred proton
 1214 mass.

1215 For the first run period of CLAS12 in the spring
 1216 and fall of 2018, the luminosity was limited to not
 1217 exceed average occupancies of 4% in the R1 drift

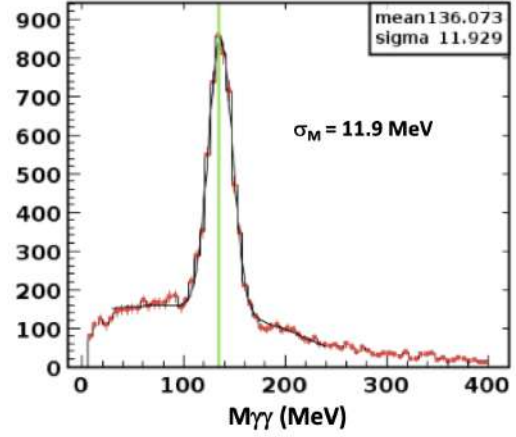


Figure 48: The invariant mass of two high-energy photons in Sector 4 of the ECAL from 10.6 GeV beam data. The background beneath the π^0 peak is due to multi-photon decays of higher-mass mesons where one or more photons are not detected in the angle range covered by the calorimeter. The width (σ) of the mass peak is 11.9 MeV, which is in good agreement with the Monte Carlo simulations in Ref. [27]. The energy calibration of the calorimeter uses cosmic ray muons.

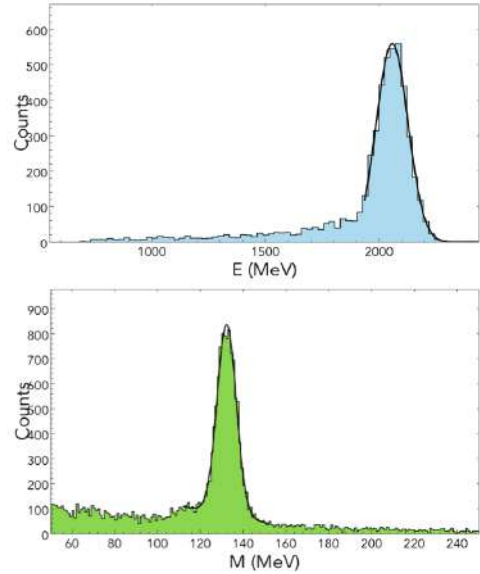


Figure 49: Top: The energy response of the FT calorimeter to elastically scattered electrons at 2.2 GeV beam energy. The tail at lower energies is due to radiative effects. The energy resolution is $\sigma_E/E \approx 3.3\%$. Bottom: 2γ mass for photons detected in the FT lead-tungstate crystal calorimeter. The π^0 mass resolution is $\sigma_{\gamma\gamma} = 4.4$ MeV, which is somewhat larger than the Monte Carlo simulation resolution of ≈ 3.5 MeV.

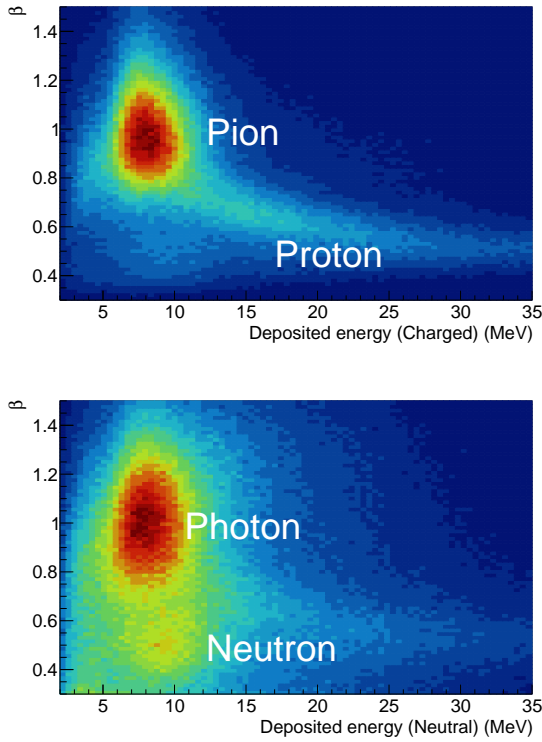


Figure 50: Top: Distribution of $\beta = v/c$ for charged particles in the CND vs. the deposited energy for correlated charged tracks in the CVT. Evidence for charged pions and protons is clearly visible. Bottom: The same for neutral particles; no charged tracks are correlated with the energy deposited in the CND scintillators.

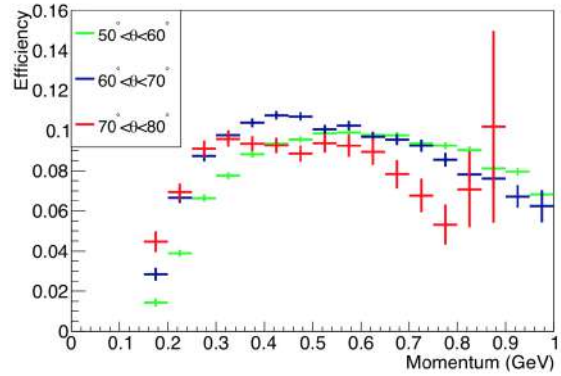


Figure 51: The neutron detection efficiency in the CND vs. momentum for different polar angles. The detection efficiency has been measured using the reaction $ep \rightarrow e'\pi^+n$, where the neutron kinematics are given by the other detected particles. The ratio of observed neutron hits to predicted neutron hits in the CND gives the detection efficiency. The efficiency has some angle and momentum dependence as shown.

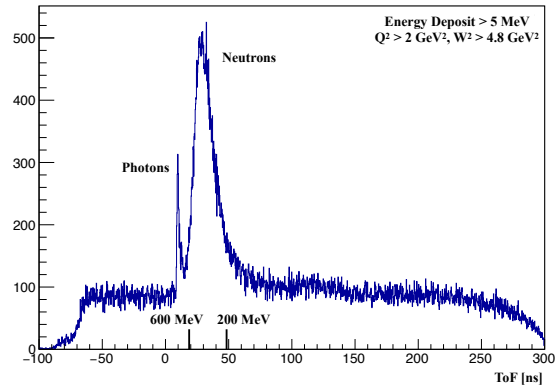


Figure 52: BAND response to electron-triggered events emerging from a nuclear target at very backward polar angles. Photons and neutrons sitting on accidental background events are well separated by precise timing information.

1218 chambers. The R1 detectors are more exposed to
 1219 background radiation than R2 and R3. This occu-
 1220 pancy limitation typically resulted in beam opera-
 1221 tions at about 45 nA to 55 nA of beam current, or
 1222 about 60% to 75% of design luminosity.

1223 *10.1.2. Performance of the RICH*

1224 Figure 57 shows the RICH multi-anode photo-
 1225 multiplier array and a single Cherenkov event for
 1226 a track with the Cherenkov light detected in the
 1227 MaPMT array. The performance in event recon-
 1228 struction is illustrated in Fig. 58 for positively charged
 1229 particles in the design momentum range from 3 to
 1230 8 GeV.

1231 *10.2. CD Reconstruction*

1232 Figure 59 shows selected charged track events in
 1233 the CVT. The left panels show the projection to the
 1234 plane perpendicular to the beamline. In this view,
 1235 positively charged particles bend clockwise in the

5 T magnetic field. The innermost 3 double layers
 mark the SVT and the outer 6 layers indicate the
 BMT. The panels to the right show the projection
 onto a plane along the beamline. The CTOF and
 CND detectors are located radially outward of the
 CVT and also show the deposited energy where the
 charged tracks hit. Uncorrelated hits are from neu-
 trals or out-of-time events. Other indicators of the

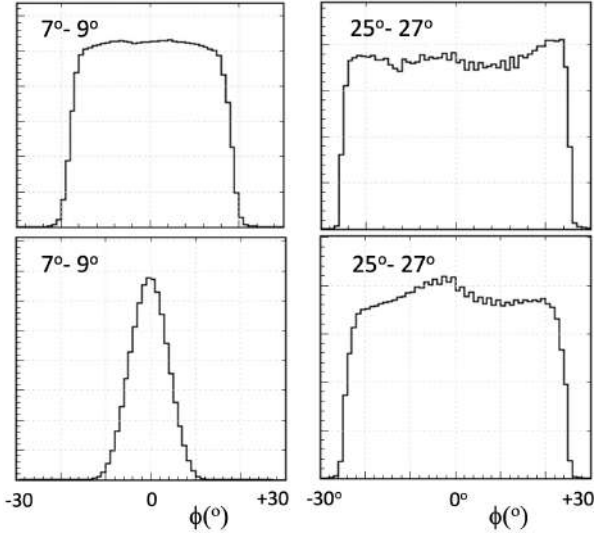


Figure 53: Yields of electrons in azimuthal angle (in deg.) for two bins in polar angle. Top: Outbending electrons, Bottom: Inbending electrons. Left: $\theta = 7^\circ - 9^\circ$. Right: $\theta = 25^\circ - 27^\circ$. The reduced ϕ acceptance at small polar angles is due to the torus coils blocking part of the ϕ coverage, as is seen in Fig. 8). In addition, for inbending electrons the acceptance is further reduced as those electrons bend towards the beamline, where the forward detectors have a smaller extension in azimuth. (The vertical axes are in arbitrary, linear units.)

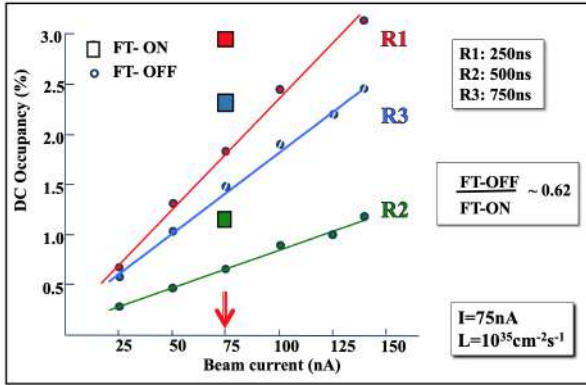


Figure 54: Accidental occupancies in the three DC regions vs. the beam current with the solenoid magnet at full field. The measurement was carried out in the FT-OFF configuration. The dependence on the beam current is linear. At 75 nA beam current the measurement was also done in the FT-ON configuration (large squares), and the accidental occupancies increase on average by $\approx 62\%$ compared to the FT-OFF configuration. The time windows during data collection were 250 ns for R1, 500 ns for R2, and 750 ns for R3, approximately corresponding to the charge collection times in the DC. The FT-ON configuration results are consistent with the Monte Carlo simulations for R1, but they underestimate the R2 data by 35% and the R3 data by 25% [24, 28].

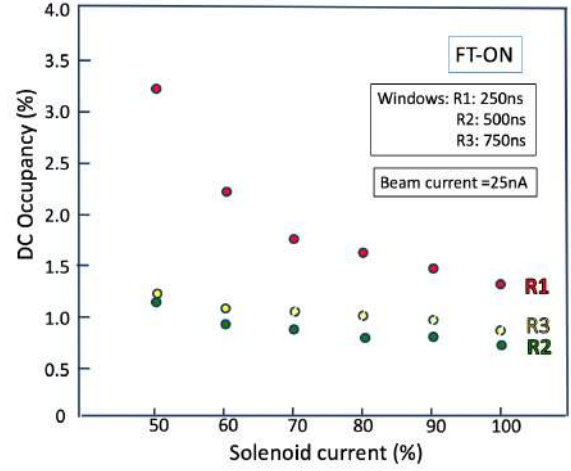


Figure 55: Hit occupancies in the three DC regions vs. the current in the solenoid magnet. The measurement was carried out in the FT-ON configuration. The sensitivity on the solenoid current comes from the fact that the primary background source is from charged particles, especially Møller electrons. The sensitivity is strongest for DC R1, which have no additional magnetic shielding from the torus magnet field, while the R2 and R3 chambers do.

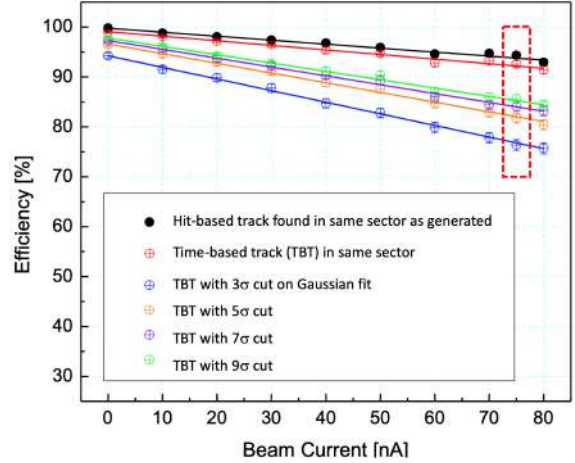


Figure 56: Single track reconstruction efficiency for simulated muon events vs. luminosity. Here the efficiency is defined as the ratio of reconstructed to generated tracks. The accidental background events were used from randomly triggered data runs taken at the same beam current. The different colored points show the tracking efficiency when certain quality constraints are imposed. About 6-7% of the tracks are lost at 75 nA beam current corresponding to a luminosity of $10^{35} \text{ cm}^{-2} \text{ s}^{-1}$ with no quality cuts (black: hit-based tracking - HBT, red: time-based tracking - TBT). The other curves show losses in the tracking efficiency when more or less stringent quality cuts are applied on the width of the missing mass distribution.

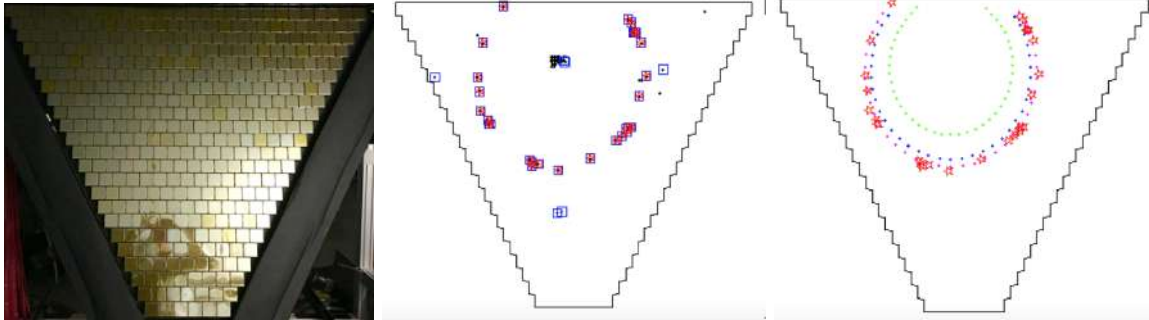


Figure 57: Photograph (left) and detector response (right) of the RICH MaPMT array during beam operation. Middle: One event with the ring of Cherenkov photons. Right: same event overlaid with expected rings from a pion, kaon, and proton at the same momentum. The radius of the Cherenkov ring is consistent with the outermost circle, which corresponds to a pion.

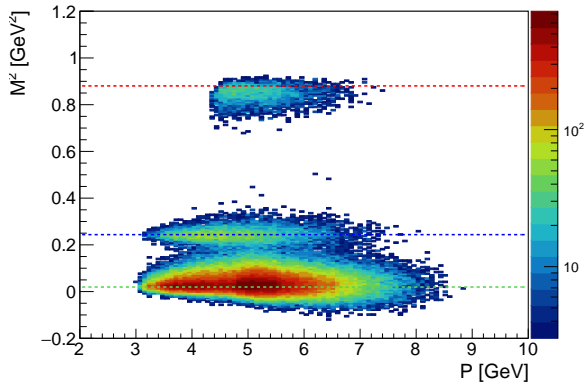


Figure 58: Charged particle identification in the RICH detector showing the mass squared vs. momentum for positively charged particles. The data show bands for π^+ (bottom), K^+ (middle), and protons (top). The events are from a single aerogel tile, and from photons that hit the MAPMT directly, without reflection from the mirrors. The pion/kaon separation in the RICH sets in where it ranges out with the time-of-flight resolution in the FTOF shown in Fig. 42.

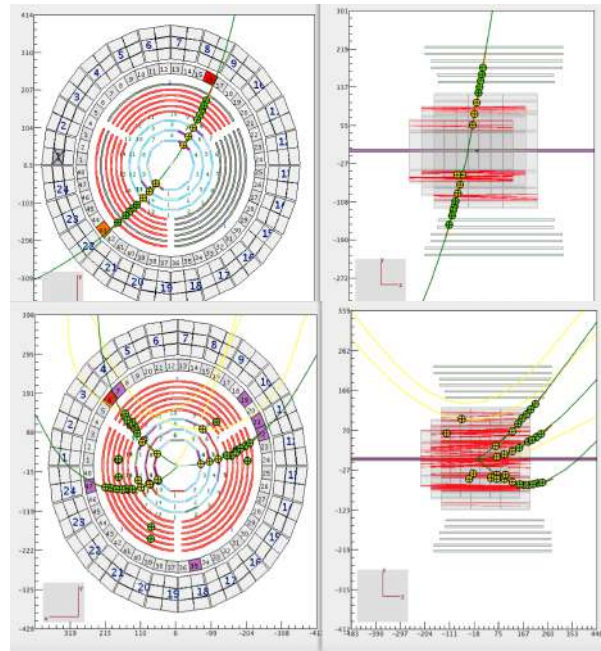


Figure 59: Top: Example of cosmic ray tracks in the CVT with magnetic field $B = 5$ T. Left: Track projected to the plane perpendicular to the beamline. Right: The same track projected onto a plane along the beamline. Bottom: Multiple track event from beam-target interaction reconstructed in the CLAS12 Central Detector at a beam current of 10 nA. Clockwise bending tracks in the solenoid magnetic field are from positively charged particles.

1245 in Fig. 60.

1246 10.2.1. Acceptance and Performance of the CD

1247 The Central Detector system covers polar angles
 1248 from 35° to 125° and the full 360° in azimuth.
 1249 Figure 61 shows the acceptance and reconstruction
 1250 efficiency for charged tracks from simulations with
 1251 background incorporated according to the beam cur-
 1252 rent. Figure 62 shows the reconstructed vertex along
 1253 the beamline (z -axis) for charged particles coming
 1254 from an empty target cell. The target cell is 5-cm
 1255 long, and the cell walls are well resolved with an
 1256 approximate resolution of $\sigma_z < 2$ mm. The final
 1257 vertex resolution should significantly improve with

the optimized detector alignment and calibrations. Events between the cell walls are from beam interactions with the residual cold hydrogen gas in the target cell.

The limited space in the CD makes charged particle identification challenging for momenta $\gtrsim 1$ GeV. The current detector performance in terms of parti-

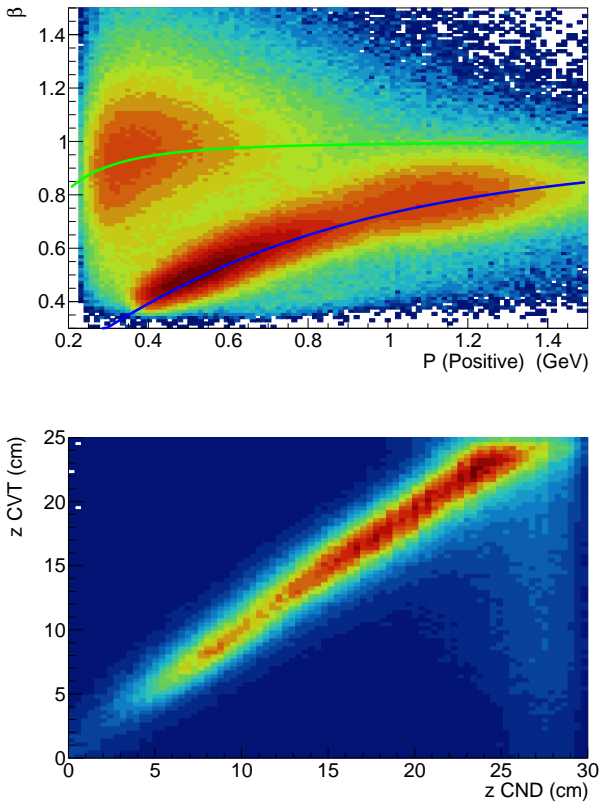


Figure 60: CND response to charged particles. The upper plot shows β vs. particle momentum for positively charged tracks. The green line indicates the nominal relation for pions and the blue line indicates the nominal relation for protons. The bottom plot shows the correlation of the hit position of charged tracks measured in the CVT and the hit position measured in the CND using the hit time information.

cle identification and tracking resolution is still being optimized and improved. It is expected that the results shown here will continue to improve and the performance will become more in agreement with the expected performance parameters.

The elastic scattering process $ep \rightarrow ep$ at relatively low Q^2 can be used to connect the FD where the electron is detected and the CD where most of the elastically scattered protons are detected. The strict kinematic correlation in azimuthal angle, given by $\phi_p = \phi_e + 180^\circ$, can be exploited to understand potential relative alignment issues between the FD and CD tracking. Figure 63 illustrates the correlation in elastic electrons detected in the FD sectors and protons reconstructed in the CD.

10.3. Operating Experience

The CLAS12 detector systems were commissioned in the period from December 2017 through February 2018, using beam energies of 2.2, 6.4, and 10.6 GeV. The target cells was filled with liquid hydrogen, except when data were taken on an empty target cell. Data were accumulated with both torus magnet polarities, i.e. electrons bending either toward or away from the beamline, as well as data with different magnetic field strength settings in the torus and solenoid. Understanding of the reconstructed events focused first on the lowest beam energy of 2.2 GeV, for which the elastic peak became quickly visible and could be used to understand the influence of the magnetic field map, the overall detector geometry, and the drift chamber alignment, among other parameters. Figure 64 shows the elastic electrons detected in each of the six different sectors of the FD to illustrate that quality of the event reconstructions and detector calibrations. After this initial commissioning period, data taking commenced for Run Group A [29], which required use of a liquid-hydrogen target. Use of hydrogen as the target material allowed for the continuation of the commissioning period, while taking production data at the same time. The ability to study exclusive processes plays an essential role in further optimizing the operational performance.

11. Summary

The design criteria, construction details, and operational performance characteristics of the large-acceptance CLAS12 dual-magnet spectrometer in Hall B at Jefferson Laboratory have been described. The spectrometer is now used to study electron-induced reactions at the energy-doubled CEBAF electron accelerator. The spectrometer was commissioned in the period from late 2017 to early 2018, and is now routinely operated in support of a diverse scientific program in the exploration of the internal quark structure of nucleons and nuclei. The major performance criteria, most critically, the operation at instantaneous luminosities up to $10^{35} \text{ cm}^{-2}\text{s}^{-1}$, have been met. These criteria are summarized in Table 2. Further improvements in the operational performance of CLAS12 will be realized during the ongoing experimental data analysis and detector optimization studies.

1327 **Acknowledgments**

1328 We acknowledge the outstanding efforts of the
 1329 staff of the Accelerator and the Nuclear Physics Di-
 1330 vision at JLab that have contributed to the de-
 1331 sign, construction, installation, and operation of
 1332 the CLAS12 detector. This work was supported
 1333 by the United States Department of Energy under
 1334 JSA/DOE Contract DE-AC05-06OR23177. This
 1335 work was also supported in part by the U.S. Na-
 1336 tional Science Foundation, the State Committee of
 1337 Science of the Republic of Armenia, the Chilean
 1338 Comisión Nacional de Investigación Científica y Tec-
 1339 nológica, the Italian Istituto Nazionale di Fisica Nu-
 1340 cleare, the French Centre National de la Recherche
 1341 Scientifique, the French Commissariat à l’Energie
 1342 Atomique, the Scottish Universities Physics Alliance
 1343 (SUPA), the United Kingdom Science and Tech-
 1344 nology Facilities Council (STFC), the National Re-
 1345 search Foundation of Korea, the Deutsche Forschungs-
 1346 gemeinschaft (DFG), and the Russian Science Foun-
 1347 dation.

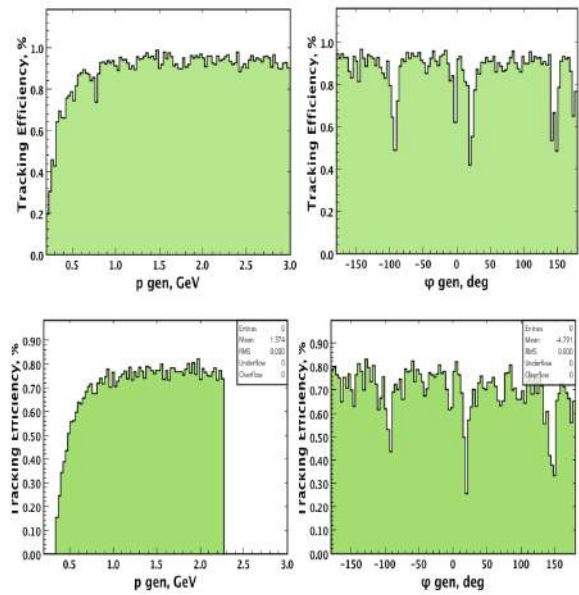


Figure 61: CVT acceptance and tracking performance. The left panels show the tracking efficiency and acceptances vs. momentum for (top) simulated muon tracks with no beam background and (bottom) the same for protons but with background corresponding to a 50 nA beam current. The right plots show the same quantities vs. azimuthal angle. The 3 ϕ angle dips are due to the support structure separating the 3 BMT segments, and are thus acceptance related. There are also small acceptance gaps between neighboring SVT modules that may account for some acceptance losses as well.

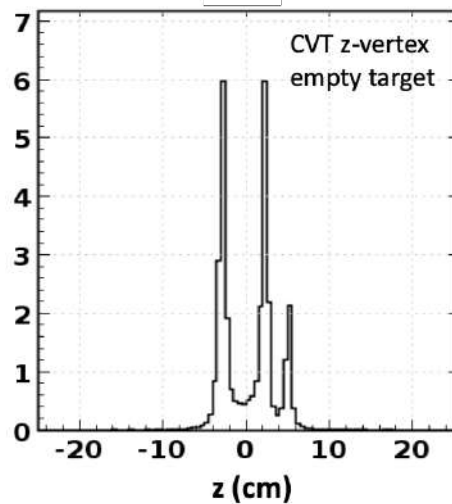


Figure 62: Reconstructed z -vertices (coordinate along the beamline) for charged tracks in the CD from an empty target cell. The cell walls are clearly visible. The small downstream peak at $z \sim 5$ cm is from events originating in a thin thermal shielding foil.

Capability	Quantity	Status
Coverage & Efficiency	Tracks (FD)	$5^\circ < \theta < 35^\circ$
	Tracks (CD)	$35^\circ < \theta < 125^\circ$
	Momentum (FD & CD)	$p > 0.2 \text{ GeV}$
	Photon angle (FD)	$5^\circ < \theta < 35^\circ$
	Photon angle (FT)	$2.5^\circ < \theta < 4.5^\circ$
	Electron detection (HTCC) Efficiency	$5^\circ < \theta < 35^\circ, 0^\circ < \phi < 360^\circ$ $\eta > 99\%$
	Neutron detection (FD) Efficiency	$5^\circ < \theta < 35^\circ$ $\leq 75\%$
	Neutron detection (CD) Efficiency	$35^\circ < \theta < 125^\circ$ 10%
Neutron Detection (BAND) Efficiency	$155^\circ < \theta < 175^\circ$ 35%	
Resolution	Momentum (FD)	$\sigma_p/p = 0.5 - 1.5\%$
	Momentum (CD)	$\sigma_p/p < 5\%$
	Pol. angles (FD)	$\sigma_\theta = 1 - 2 \text{ mrad}$
	Pol. angles (CD)	$\sigma_\theta = 10 - 20 \text{ mrad}$
	Azim. angles (FD)	$\sigma_\phi < 1 \text{ mrad}/\sin \phi$
	Azim. angles (CD)	$\sigma_\phi < 1 \text{ mrad}$
	Timing (FD)	$\sigma_T = 60 - 110 \text{ ps}$
	Timing (CD)	$\sigma_T = 80 - 100 \text{ ps}$
	Energy (σ_E/E) (FD)	$0.1/\sqrt{E} \text{ (GeV)}$
	Energy (σ_E/E) (FT)	$0.03/\sqrt{E} \text{ (GeV)}$
Operation	Luminosity	$L = 10^{35} \text{ cm}^{-2}\text{s}^{-1}$
DAQ	Data Rate	20 kHz, 800 MB/s., L.T. 95%
Magnetic Field	Solenoid	$B_0 = 5 \text{ T}$
	Torus	$\int B dl = 0.5 - 2.7 \text{ Tm}$ at $5^\circ < \theta < 25^\circ$

Table 2: CLAS12 performance parameters based on the current state of the reconstruction, subsystem calibrations, knowledge of the detector misalignments, and the understanding of the torus and solenoid magnetic fields.

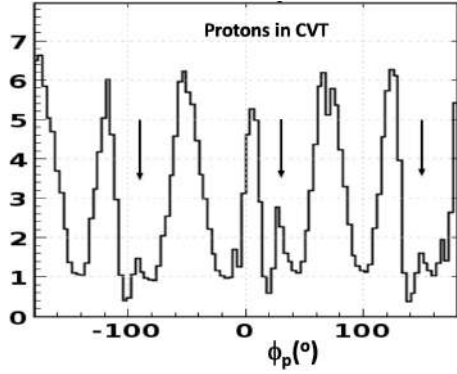


Figure 63: Elastically scattered protons reconstructed in the CVT and CTOF. The proton peaks show the reflection of the 6 FD sectors where the electrons are detected. In addition there is a 3-fold modulation (seen in the different widths of 3 of the peaks) due to the 3 BMT sectors where protons are detected. The arrows indicate the physical position of the support structures at the boundaries between two BMT segments. The azimuthal angle is the reconstructed angle at the production target. Due to the clockwise curvature of proton tracks in the solenoid magnetic field (see bottom plot in Fig. 59) the support structures appear shifted by a certain $\Delta\phi_p$ amount relative to their locations in the lab. (The vertical axes is in arbitrary units).

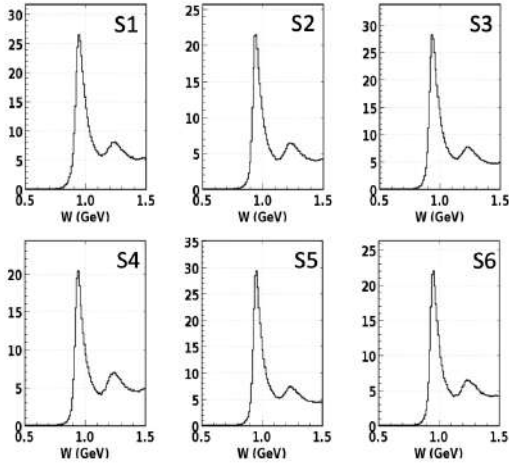


Figure 64: Elastically scattered electrons off protons from 2.2 GeV data in all of the FD sectors showing the reconstructed W distributions.

References

- 1348
1349
1350
1351
1352
1353
1354
1355
1356
1357
1358
1359
1360
1361
1362
1363
1364
1365
1366
1367
1368
1369
1370
1371
1372
1373
1374
1375
1376
1377
1378
1379
1380
1381
1382
1383
1384
1385
1386
1387
1388
1389
1390
1391
1392
1393
1394
1395
1396
1397
1398
1399
1400
1401
1402
1403
1404
1405
1406
1407
1408
1409
1410
1411
- [1] R. W. McAllister and R. Hofstadter, “*Elastic Scattering of 188-MeV Electrons From the Proton and the α Particle*”, Phys. Rev. **102**, 851 (1956). doi:10.1103/PhysRev.102.851
- [2] M. Breidenbach *et al.*, “*Observed Behavior of Highly Inelastic electron-Proton Scattering*”, Phys. Rev. Lett. **23**, 935 (1969). doi:10.1103/PhysRevLett.23.935
- [3] S. E. Kuhn, J.-P. Chen, and E. Leader, “*Spin Structure of the Nucleon - Status and Recent Results*”, Prog. Part. Nucl. Phys. **63**, 1 (2009) doi:10.1016/j.pppnp.2009.02.001.
- [4] C. W. Leemann, D. R. Douglas, and G. A. Krafft, “*The Continuous Electron Beam Accelerator Facility: CEBAF at the Jefferson Laboratory*”, Ann. Rev. Nucl. Part. Sci. **51**, 413 (2001). doi:10.1146/annurev.nucl.51.101701.132327
- [5] B. A. Mecking *et al.*, “*The CEBAF Large Acceptance Spectrometer (CLAS)*”, Nucl. Instrum. Meth. A **503** (2003). doi:10.1016/S0168-9002(03)01001-5
- [6] V. D. Burkert, “*Jefferson Lab at 12 GeV: The Science Program*”, Ann. Rev. Nucl. Part. Sci. **68**, 405 (2018). doi:10.1146/annurev-nucl-101917-021129
- [7] R. Fair *et al.*, “*The CLAS12 Superconducting Magnets*”, to be published in Nucl. Inst. and Meth. A, (2020). (see this issue)
- [8] M.D. Mestayer *et al.*, “*The CLAS12 Drift Chamber System*”, to be published in Nucl. Inst. and Meth. A, (2020). (see this issue)
- [9] Y.G. Sharabian *et al.*, “*The CLAS12 High Threshold Cherenkov Counter*”, to be published in Nucl. Inst. and Meth. A, (2020). (see this issue)
- [10] G. Adams *et al.*, “*The CLAS Cherenkov detector*”, Nucl. Instrum. Meth. A **465**, 414 (2001). doi:10.1016/S0168-9002(00)01313-9
- [11] M. Ungaro *et al.*, “*The CLAS12 Low Threshold Cherenkov Counter*”, to be published in Nucl. Inst. and Meth. A, (2020). (see this issue)
- [12] M. Contalbrigo *et al.*, “*The CLAS12 Ring Imaging Cherenkov Detector*”, to be published in Nucl. Inst. and Meth. A, (2020). (see this issue)
- [13] D.S. Carman *et al.*, “*The CLAS12 Forward Time-of-Flight System*”, to be published in Nucl. Inst. and Meth. A, (2020). (see this issue)
- [14] M. Amarian *et al.*, “*The CLAS Forward Electromagnetic Calorimeter*”, Nucl. Instrum. Meth. A **460**, 239 (2001). doi:10.1016/S0168-9002(00)00996-7
- [15] G. Asryan *et al.*, “*The CLAS12 Forward Electromagnetic Calorimeter*”, to be published in Nucl. Inst. and Meth. A, (2020). (see this issue)
- [16] A. Acker *et al.*, “*The CLAS12 Forward Tagger*”, to be published in Nucl. Inst. and Meth. A, (2020). (see this issue)
- [17] M. A. Antonioli *et al.*, “*The CLAS12 Silicon Vertex Tracker*”, to be published in Nucl. Inst. and Meth. A, (2020). (see this issue)
- [18] F. Bossu *et al.*, “*The CLAS12 Micromegas Vertex Tracker*”, to be published in Nucl. Inst. and Meth. A, (2020). (see this issue)
- [19] V. Baturin *et al.*, “*Dynamic magnetic shield for the CLAS12 central TOF detector photomultiplier tubes*”, Nucl. Instrum. Meth. A **664** (2012)11, doi:10.1016/j.nima.2011.10.003
- [20] D.S. Carman *et al.*, “*The CLAS12 Central Time-of-Flight System*”, to be published in Nucl. Inst. and Meth. A, (2020). (see this issue)
- [21] P. Chatagnon *et al.*, “*The CLAS12 Central Neutron Detector*”, to be published in Nucl. Inst. and Meth. A, (2020). (see this issue)
- [22] The CLAS12 Back Angle Neutron Detector (BAND), NIM article in preparation.
- [23] N. Baltzell *et al.*, “*The CLAS12 Beamline and its Performance*”, to be published in Nucl. Inst. and Meth. A, (2020). (see this issue)
- [24] M. Ungaro *et al.*, “*The CLAS12 Geant4 Simulation*”, to be published in Nucl. Inst. and Meth. A, (2020). (see this issue)
- [25] S. Boyarinov *et al.*, “*The CLAS12 Data Acquisition System*”, to be published in Nucl. Inst. and Meth. A, (2020). (see this issue)
- [26] B. Raydo *et al.*, “*The CLAS12 Trigger System*”, to be published in Nucl. Inst. and Meth. A, (2020). (see this issue)
- [27] V. Ziegler *et al.*, “*The CLAS12 Software Framework and Event Reconstruction*”, to be published in Nucl. Inst. and Meth. A, (2020). (see this issue)
- [28] V. Burkert, S. Stepanyan, J. A. Tan, and M. Ungaro, CLAS12 Note 2017-018, (2017). <https://misportal.jlab.org/mis/physics/clas12/viewFile.cfm/2017-018.pdf?documentId=54>.
- [29] CLAS12 Run Groups, https://www.jlab.org/Hall-B/clas12-web/Hall_B_experiment_run_groups.pdf